A reduced basis method for parametrized variational inequalities applied to contact mechanics

Amina Benaceur, Alexandre Ern, Virginie Ehrlacher

To cite this version:

Amina Benaceur, Alexandre Ern, Virginie Ehrlacher. A reduced basis method for parametrized variational inequalities applied to contact mechanics. International Journal for Numerical Methods in Engineering, 2019, 10.1002/nme.6261 . hal-02081485v3

A reduced basis method for parametrized variational inequalities applied to contact mechanics[*]

Amina Benaceur[†][‡], Alexandre Ern[†], Virginie Ehrlacher[†]

Abstract

We investigate new developments of the Reduced-Basis (RB) method for parametrized optimization problems with nonlinear constraints. We propose a reduced-basis scheme in a saddle-point form combined with the Empirical Interpolation Method to deal with the nonlinear constraint. In this setting, a primal reduced-basis is needed for the primal solution and a dual one is needed for the Lagrange multipliers. We suggest to construct the latter using a cone-projected greedy algorithm that conserves the non-negativity of the dual basis vectors. The reduction strategy is applied to elastic frictionless contact problems including the possibility of using non-matching meshes. The numerical examples confirm the efficiency of the reduction strategy.

1 Introduction

The Reduced-Basis (RB) method [1, 2] is a computationally effective approach to approximate the solution of parametrized Partial Differential Equations (PDEs) in multi-query and real-time contexts, where the problem has to be solved repeatedly for a large number of parameter values or needs to be solved very quickly under limited computational resources. For standard PDEs in variational form, RB methods provide efficient tools for complexity reduction. Instead of the High-Fidelity (HF) problem, which is high-dimensional after a finite element discretization, a low-dimensional model is generated. This low-dimensional problem can then be solved significantly faster for a wide range of parameters.

The focus here is on parametrized optimization problems with nonlinear constraints. These problems are of great importance in numerous engineering applications. Owing to the nonlinearity of the constraints, the algorithms designed for solving these problems often suffer from slow convergence, thereby entailing subsequent computational costs. Therefore, there is a strong motivation for devising RB methods for nonlinear constrained optimization problems. The literature on RB methods for variational inequalities with linear constraints is already relatively abundant. In [3], the authors extend the standard RB method to linear variational inequalities solved through a mixed formulation. The primal basis (for the primal solution) and the dual one (for the Lagrange multipliers) are constructed using well-chosen snapshots, and no additional compression phase is considered. In the so-called

---

[*] This work is partially supported by Electricité De France (EDF) and a CIFRE PhD fellowship from ANRT.

[†] University Paris-Est, CERMICS (ENPC), 77455 Marne la Vallée Cedex 2 and INRIA Paris, 75589 Paris, France.

[‡] EDF Lab Les Renardières, 77250 Ecuelles Cedex, France.

The authors are thankful to M. Abbas, S. Meunier and J.-F. Rit (EDF Lab) for stimulating discussions, and to the reviewers for their comments.

Projection-Based method of [4], which has been specifically introduced to address time-dependent contact problems with linear constraints, the primal and the dual spaces are built differently: the primal RB space is obtained using Proper Orthogonal Decomposition (POD), whereas the dual one is built by applying the Non-negative Matrix Factorization (NMF) algorithm [5] to the set of Lagrange multiplier snapshots. The NMF guarantees non-negative basis vectors and a user-prescribed RB dimension, but the resulting dual RB space can be (far) less accurate than the primal one. As a matter of fact, the user does not specify a required error tolerance as an input but a number of dominant basis vectors to retain. The work in [6] extends hyper-reduction methods to contact problems with linear constraints. The proposed extension consists in conserving a few vectors of the High-Fidelity (HF) dual basis because the number of contact nodes is limited to a reduced integration domain. Hence, only the contact nodes in this domain are treated but with a local high fidelity. Further relevant work for RB methods and variational inequalities with linear constraints comprises [7, 8], which address time-space formulations and corresponding analysis. Also, [9] treats the inequality constraints using the primal-dual strategy, and [10, 11] develop related empirical interpolation for a penalty formulation and subsequent error estimation. We finally mention [12, 13, 14] which are related to [3] and have dealt with RB methods for stationary variational inequalities treating non-stationary problems and providing *a posteriori* error estimations for financial applications. An angle-greedy algorithm which is used for the construction of the dual basis is also introduced therein. So far, all the existing results using the RB method deal with linear constraints. Yet, we mention that another class of model order reduction methods, namely the Proper Generalized Decomposition (PGD), is used in [15] to address nonlinear contact problems.

In this paper, we propose to extend model reduction to the framework of variational inequalities with nonlinear constraints. An important application we have in mind is elastic frictionless contact in a generic framework. Importantly, we want to circumvent two simplifying assumptions often made in the literature: the small displacement assumption (that allows one to consider the same normal vector on both contact boundaries) and the use of non-matching meshes (which is not realistic in many engineering scenarios). As a result, we are dealing with nonlinear constraints. We express the problem of interest in a saddle-point form using Lagrange multipliers, and we apply the Empirical Interpolation Method (EIM) [16, 17] to allow for an offline/online decomposition of the nonlinear constraints. The primal RB space is constructed using POD (alternative options based, e.g., on a greedy algorithm can also be considered), whereas we devise a Cone-Projected Greedy (CPG) algorithm that builds nested dual RB spaces while preserving the non-negativity of the Lagrange multipliers. More precisely, the CPG algorithm enriches the dual cone at each iteration using the Lagrange multiplier that maximizes the positive projection on the previously selected cone. The CPG algorithm is closely related to the angle-greedy algorithm from [14]. The selection criterion remains somewhat different since the former is based on positive cone projections and the latter on linear projections. A more detailed comparison is presented in Section 5.

This paper is organized as follows. In Section 2, we introduce the abstract model problem. In Section 3, we consider more specifically elastic frictionless contact problems. Since we do not make the simplifying hypotheses discussed above, we briefly describe the formulation of the nonlinear non-interpenetration condition. In Section 4, we return to the abstract setting and we apply the RB method to derive the reduced-order problem. In Section 5, we discuss the offline stage in some detail, we present the EIM procedure for the nonlinear constraint, and we describe the construction of the primal and dual RB spaces. In Section 6, we present numerical results illustrating the performance of the method in the framework of elastic frictionless contact. We consider two test cases. First, the contact problem between two disks introduced by Hertz [18] with a parametrization either on the prescribed displacement of the disks or on the radius of the lower disk. Then, the case of a ring with a parameter-dependent radius in contact with a rectangular block [19]. Finally, Section 7 draws some conclusions.

2 Model problem

Let $\mathcal{V}$ be a separable Hilbert space composed of functions defined on a spatial domain (open, bounded, connected subset) $\Omega \subset \mathbb{R}^d$, $d \geqslant 1$, with a Lipschitz boundary $\partial\Omega$. Let $\overline{\Omega}$ denote the closure of Ω and let $\mathcal{P}$ denote a parameter set. We define a continuous, symmetric and coercive bilinear form $a : \mathcal{P} \times \mathcal{V} \times \mathcal{V} \to \mathbb{R}$ (the attributes of a are with respect to its second and third arguments), and a continuous linear form $f : \mathcal{P} \times \mathcal{V} \to \mathbb{R}$ (the attributes of f are with respect to its second argument). We also define the nonlinear continuous mappings $k : \mathcal{P} \times \mathcal{V} \times \mathcal{V} \to L^2(\Gamma^c)$ and $g : \mathcal{P} \times \mathcal{V} \to L^2(\Gamma^c)$, for a subset $\Gamma^c \subset \partial\Omega$. For simplicity, we consider at this stage that the domain Ω and the subset Γ^c are parameter-independent. A more general setting with parameter-dependent $\Omega(\mu)$ and $\Gamma^c(\mu)$ will be considered from Section 3 onwards.

For all $\mu \in \mathcal{P}$, we want to solve the following nonlinear minimization problem: Find $u(\mu) \in \mathcal{V}$ such that

$$\begin{cases} u(\mu) = \underset{v \in \mathcal{V}}{\operatorname{argmin}} \ \dfrac{1}{2} a(\mu; v, v) - f(\mu; v) \\ k(\mu, u(\mu); u(\mu)) \leqslant g(\mu, u(\mu)) \quad \text{a.e. on } \Gamma^c. \end{cases} \tag{1}$$

In (1), the dependency is nonlinear with respect to the arguments before the semicolon and linear with respect to the arguments after it.

Remark 1 (Nonlinear constraint). *The nonlinear constraint in* (1) *can be formulated more compactly as* $\zeta(\mu, u(\mu)) \leqslant 0$ *for the nonlinear continuous mapping* $\zeta(\mu, v) : \mathcal{P} \times \mathcal{V} \to L^2(\Gamma^c)$ *defined as*

$$\zeta(\mu, v) := k(\mu, v; v) - g(\mu, v). \tag{2}$$

The adopted decomposition of $\zeta(\mu, v)$ *in* (2) *is natural in the context of elastic frictionless contact problems. Note that this decomposition is not unique since one can write* $\zeta(\mu, v) = \tilde{k}(\mu, v; v) - \tilde{g}(\mu, v)$ *with* $\tilde{k}(\mu, v; v) := k(\mu, v; v) + \delta(\mu, v; v)$, $\tilde{g}(\mu, v) := g(\mu, v) + \delta(\mu, v; v)$, *and an arbitrary mapping* $\delta(\mu, v; v) : \mathcal{P} \times \mathcal{V} \times \mathcal{V} \to L^2(\Gamma^c)$.

The present setting is motivated by elastic frictionless contact problems that will be described in more detail in Section 3. We make three assumptions. First, we assume that the inequality constraint in (1) is quasi-linear, i.e., that k is linear with respect to its third argument. This assumption, which is not fundamental, will be exploited below in setting up an iterative solver for the discrete version of (1). Second, we assume that g satisfies $g(\mu, 0) \geqslant 0$. Hence, the set of admissible states

$$\mathcal{K} = \{v \in \mathcal{V} \mid k(\mu, v; v) \leqslant g(\mu, v)\} \tag{3}$$

is non-empty since $0 \in \mathcal{K}$. Third, we assume that the problem (1) is well-posed. Note that the functional minimized in (1) is strongly convex and continuous, and the set $\mathcal{K}$ is closed owing to the continuity of k and g. Therefore, the existence of a minimizer is guaranteed. Our third assumption then means that we assume the uniqueness of the searched minimizer in $\mathcal{K}$. The well-posedness assumption is extended to all the formulations derived from (1) in the remainder of the paper, namely, the assumption applies to the saddle-point formulation (5), its finite element approximation (9), its linearized version (9), and its RB approximation (43).

We consider the non-empty closed convex cone $\mathcal{W}^+ := L^2(\Gamma^c;\mathbb{R}_+)$, with $\mathbb{R}_+ := [0,+\infty)$. Using the test cone $\mathcal{W}^+$, the weak form of the inequality constraint in (1) reads as follows:

$$\int_{\Gamma^c} k(\mu, u(\mu); u(\mu))\eta \leqslant \int_{\Gamma^c} g(\mu, u(\mu))\eta, \quad \forall \eta \in \mathcal{W}^+. \tag{4}$$

Using a Lagrangian formulation, the constrained minimization problem (1) is rewritten as a saddle-point problem: Find $(u(\mu), \lambda(\mu)) \in \mathcal{V} \times \mathcal{W}^+$ such that

$$(u(\mu), \lambda(\mu)) = \arg \underset{v\in\mathcal{V},\eta\in\mathcal{W}^+}{\mathrm{minmax}}\ \mathcal{L}(\mu)(v,\eta), \tag{5}$$

where the Lagrangian $\mathcal{L}(\mu) : \mathcal{V} \times \mathcal{W}^+ \to \mathbb{R}$ is defined as

$$\mathcal{L}(\mu)(v,\eta) := \frac{1}{2}a(\mu; v, v) - f(\mu; v) + \left(\int_{\Gamma^c} k(\mu, v; v)\eta - \int_{\Gamma^c} g(\mu, v)\eta\right), \tag{6}$$

and $u(\mu)$ and $\lambda(\mu)$ are respectively called the primal and the dual solutions of the saddle-point problem (5).

To discretize (5) in space, one typically uses a conforming Finite Element Method (FEM) [20] for the primal variable and discontinuous functions for the dual variable. Both variables are defined using the same background mesh, but in some cases the basis functions for the dual variable can have a slightly larger support than those for the primal variable. The FEM is based on a finite element subspace $V_{\mathcal{N}} := \mathrm{span}\{\phi_1, \ldots, \phi_{\mathcal{N}}\} \subsetneq \mathcal{V}$ defined using a mesh based on a discrete nodal subset $\Omega^{\mathrm{tr}} \subsetneq \overline{\Omega}$, where $\mathrm{Card}(\Omega^{\mathrm{tr}}) = \mathcal{N}$. Besides, one introduces the subcone $W^+_{\mathcal{R}} := \mathrm{span}_+\{\psi_1, \ldots, \psi_{\mathcal{R}}\} \subsetneq \mathcal{W}^+$ defined using a discrete nodal subset $\Gamma^{c,\mathrm{tr}} \subsetneq \Gamma^c$, where $\mathrm{Card}(\Gamma^{c,\mathrm{tr}}) = \mathcal{R}$. The notation span_+ means that linear combinations are restricted to non-negative coefficients. The discrete saddle-point problem reads: Find $(u_{\mathcal{N}}(\mu), \lambda_{\mathcal{R}}(\mu)) \in V_{\mathcal{N}} \times W^+_{\mathcal{R}}$ such that

$$(u_{\mathcal{N}}(\mu), \lambda_{\mathcal{R}}(\mu)) = \arg \underset{v\in V_{\mathcal{N}},\eta\in W^+_{\mathcal{R}}}{\mathrm{minmax}}\ \mathcal{L}(\mu)(v,\eta), \tag{7}$$

with the Lagrangian defined in (6). Note that the discrete inequality constraint amounts to

$$\int_{\Gamma^c} k(\mu, u_{\mathcal{N}}(\mu); u_{\mathcal{N}}(\mu))\psi_r \leqslant \int_{\Gamma^c} g(\mu, u_{\mathcal{N}}(\mu))\psi_r, \quad \forall r \in \{1, \ldots, \mathcal{R}\}. \tag{8}$$

As is customary with the RB method, we assume henceforth that the mesh-size is small enough so that the above space discretization method delivers HF primal and dual solutions within the desired level of accuracy. Introducing the component vectors $\mathbf{u}(\mu) := (u_n(\mu))_{1\leqslant n\leqslant\mathcal{N}} \in \mathbb{R}^{\mathcal{N}}$ and $\boldsymbol{\lambda}(\mu) := (\lambda_r(\mu))_{1\leqslant r\leqslant\mathcal{R}} \in \mathbb{R}^{\mathcal{R}}_+$ of $u_{\mathcal{N}}(\mu)$ and $\lambda_{\mathcal{N}}(\mu)$ respectively, the algebraic formulation of (7) reads: Find $(\mathbf{u}(\mu), \boldsymbol{\lambda}(\mu)) \in \mathbb{R}^{\mathcal{N}} \times \mathbb{R}^{\mathcal{R}}_+$ satisfying

$$(\mathbf{u}(\mu), \boldsymbol{\lambda}(\mu)) = \arg \underset{\mathbf{v}\in\mathbb{R}^{\mathcal{N}},\boldsymbol{\eta}\in\mathbb{R}^{\mathcal{R}}_+}{\mathrm{minmax}}\ \frac{1}{2}\mathbf{v}^T\mathbf{A}(\mu)\mathbf{v} - \mathbf{v}^T\mathbf{f}(\mu) + \boldsymbol{\eta}^T\big(\mathbf{K}(\mu,\mathbf{v})\mathbf{v} - \mathbf{g}(\mu,\mathbf{v})\big), \tag{9}$$

with the matrices $\mathbf{A}(\mu) \in \mathbb{R}^{\mathcal{N}\times\mathcal{N}}$ and $\mathbf{K}(\mu,\mathbf{w}) \in \mathbb{R}^{\mathcal{R}\times\mathcal{N}}$ such that

$$\begin{cases} \mathbf{A}(\mu)_{ij} := a(\mu; \phi_j, \phi_i), \\ \mathbf{K}(\mu,\mathbf{w})_{rj} := \displaystyle\int_{\Gamma^c} k(\mu, w; \phi_j)\psi_r, \end{cases} \tag{10}$$

and the vectors $\mathbf{f}(\mu) \in \mathbb{R}^{\mathcal{N}}$ and $\mathbf{g}(\mu, \mathbf{w}) \in \mathbb{R}^{\mathcal{R}}$ such that

$$\begin{cases} \mathbf{f}(\mu)_j := f(\mu; \phi_j), \\ \mathbf{g}(\mu, \mathbf{w})_r := \displaystyle\int_{\Gamma^c} g(\mu, \mathbf{w}) \psi_r. \end{cases} \tag{11}$$

In the sequel, we will solve (9) using an iterative algorithm, where the terms $\mathbf{K}(\mu, \mathbf{v})$ and $\mathbf{g}(\mu, \mathbf{v})$ are treated explicitly. This amounts to a so-called secant method or Kačanov iterative method [21]. The Kačanov method consists in solving the following problems : For all $k \geqslant 1$,

$$\begin{aligned} (\mathbf{u}^k(\mu), \boldsymbol{\lambda}^k(\mu)) = \arg \min_{\mathbf{v} \in \mathbb{R}^{\mathcal{N}}, \eta \in \mathbb{R}^{\mathcal{R}}_+} \max \; & \frac{1}{2} \mathbf{v}^T \mathbf{A}(\mu) \mathbf{v} - \mathbf{v}^T \mathbf{f}(\mu) \\ & + \boldsymbol{\eta}^T \big(\mathbf{K}(\mu, \mathbf{u}^{k-1}(\mu)) \mathbf{v} - \mathbf{g}(\mu, \mathbf{u}^{k-1}(\mu)) \big). \end{aligned} \tag{12}$$

For a user-defined tolerance $\epsilon_{\text{KA}} > 0$, the stopping criterion of the Kačanov method reads

$$\frac{\| \mathbf{u}^k(\mu) - \mathbf{u}^{k-1}(\mu) \|_{\mathbb{R}^{\mathcal{N}}}}{\| \mathbf{u}^{k-1}(\mu) \|_{\mathbb{R}^{\mathcal{N}}}} \leqslant \epsilon_{\text{KA}}. \tag{13}$$

Depending on the problem and output of interest, an additional check on the dual increment $\| \boldsymbol{\lambda}^k(\mu) - \boldsymbol{\lambda}^{k-1}(\mu) \|_{\mathbb{R}^{\mathcal{R}}} / \| \boldsymbol{\lambda}^{k-1}(\mu) \|_{\mathbb{R}^{\mathcal{R}}}$ can be performed. The advantage of the Kačanov method is its simplicity. Indeed, unlike the standard Newton method, the Kačanov method does not require any computation of Jacobian preconditioners, thereby achieving significant computational savings when solving (9). However, if the Newton method converges, it is (much) faster than the Kačanov method. In Section 4, the reduced problem will be solved using the Kačanov method as well. Therein, we will shortly discuss the influence of the solver on the reduction scheme (cf. Remark 5).

3 Prototypical example: elastic frictionless contact

The model reduction of mechanical problems involving contact remains an important issue in computational solid mechanics. In this section, we consider the case of elastic frictionless contact, and we detail how this problem can be recast in the form (1). Let us mention that the domains occupied by the solids are allowed to be parameter-dependent.

3.1 Linear elasticity

For all $\mu \in \mathcal{P}$, the domain $\Omega(\mu) \subset \mathbb{R}^d$, $d \in \{2, 3\}$, represents the initial configuration of a deformable medium initially at equilibrium and to which an external load $\ell(\mu) : \Omega(\mu) \to \mathbb{R}^d$ is applied. We use tildes to denote fields defined on this configuration. We define the functional space $\mathcal{V}(\mu)$ such that

$$\mathcal{V}(\mu) := H^1(\Omega(\mu); \mathbb{R}^d). \tag{14}$$

For all $\tilde{v} \in \mathcal{V}(\mu)$, let $\varepsilon(\tilde{v}) \in \mathbb{R}^{d \times d}$ be the linearized strain tensor defined as

$$\varepsilon(\tilde{v}) := \frac{1}{2} (\nabla \tilde{v} + \nabla \tilde{v}^T). \tag{15}$$

In the framework of linear isotropic elasticity, the stress tensor $\sigma(\widetilde{v}) \in \mathbb{R}^{d\times d}$ is related to the linearized strain tensor by the formula

$$\sigma(\widetilde{v}) = \frac{E\nu}{(1+\nu)(1+2\nu)}\operatorname{tr}(\varepsilon(\widetilde{v}))\mathcal{I} + \frac{E}{(1+\nu)}\varepsilon(\widetilde{v}), \tag{16}$$

where E is the Young modulus, ν is the Poisson coefficient and $\mathcal{I}$ is the identity tensor in $\mathbb{R}^{d\times d}$. For simplicity, we have supposed that E and ν are parameter-independent. The standard linear elasticity problem consists in finding the displacement field $\widetilde{u}(\mu) : \Omega(\mu) \to \mathbb{R}^d$ induced by the externally applied force field $\ell(\mu) : \Omega(\mu) \to \mathbb{R}^d$ once the system has reached equilibrium:

$$\nabla \cdot \sigma(\widetilde{u}(\mu)) = \ell(\mu) \quad \text{in } \Omega(\mu). \tag{17}$$

This leads to the parameter-dependent bilinear form $\widetilde{a} : \mathcal{P} \times \mathcal{V}(\mu) \times \mathcal{V}(\mu) \to \mathbb{R}$ such that

$$\widetilde{a}(\mu; \widetilde{v}, \widetilde{w}) := \int_{\Omega(\mu)} \sigma(\widetilde{v}) : \varepsilon(\widetilde{w}), \tag{18}$$

and the parameter-dependent linear form $\widetilde{f} : \mathcal{P} \times \mathcal{V}(\mu) \to \mathbb{R}$ such that

$$\widetilde{f}(\mu; \widetilde{w}) := \int_{\Omega(\mu)} \ell(\mu) \cdot \widetilde{w}. \tag{19}$$

3.2 Non-interpenetration condition

We formulate the non-interpenetration condition in a general framework without restricting ourselves to the small displacement assumption. For simplicity, we consider two elastic bodies. Thus, the domain $\Omega(\mu)$ can be partitioned as

$$\overline{\Omega}(\mu) = \overline{\Omega}_1(\mu) \cup \overline{\Omega}_2(\mu) \qquad \text{with} \qquad \Omega_1(\mu) \cap \Omega_2(\mu) = \varnothing,$$

where $\Omega_1(\mu)$ and $\Omega_2(\mu)$ represent the initial configuration of the two disjoint deformable solids. For all $\mu \in \mathcal{P}$, let $\Gamma_1^c(\mu)$ and $\Gamma_2^c(\mu)$ be the potential contact boundaries of $\Omega_1(\mu)$ and $\Omega_2(\mu)$ respectively. For all $\widetilde{v} \in \mathcal{V}(\mu)$ and all $i \in \{1, 2\}$, we introduce the functions $\widetilde{v}_i : \Omega_i(\mu) \to \mathbb{R}^d$ such that

$$\widetilde{v}_i := \widetilde{v}_{|\Omega_i(\mu)} \in H^1(\Omega_i(\mu); \mathbb{R}^d). \tag{20}$$

In order to formulate the non-interpenetration condition, we introduce some auxiliary geometric mappings. An illustration is given in Figure 1. For all $\mu \in \mathcal{P}$, all $\widetilde{v} \in \mathcal{V}(\mu)$ and all $i \in \{1, 2\}$, we define the geometric mappings

$$\begin{aligned} \psi_i(\mu, \widetilde{v}_i) :\ \Gamma_i^c(\mu) &\to \Upsilon_i^c(\mu, \widetilde{v}_i) \\ z &\mapsto z + \widetilde{v}_i(z), \end{aligned} \tag{21}$$

where $\Upsilon_i^c(\mu, \widetilde{v}_i) := \psi_i(\mu, \widetilde{v}_i)\big(\Gamma_i^c(\mu)\big)$. As is often the case in the context of solid mechanics, we assume that auto-contact and auto-penetration are excluded, i.e., two different points of the same body are bound to occupy two disjoint points in space, so that the mapping $\psi_i(\mu, \widetilde{v}_i)$ is injective. Therefore, $(\psi_i(\mu, \widetilde{v}_i))^{-1} : \Upsilon_i^c(\mu, \widetilde{v}_i) \to \Gamma_i^c(\mu)$ is well defined. We further assume that the contact mapping

$$\begin{aligned} \vartheta(\mu, \widetilde{v}) : \Upsilon_1^c(\mu, \widetilde{v}_1) &\to \Upsilon_2^c(\mu, \widetilde{v}_2) \\ z_1 &\mapsto \operatorname*{argmin}_{z_2 \in \Upsilon_2^c(\mu, \widetilde{v}_2)} \|z_1 - z_2\|, \end{aligned} \tag{22}$$

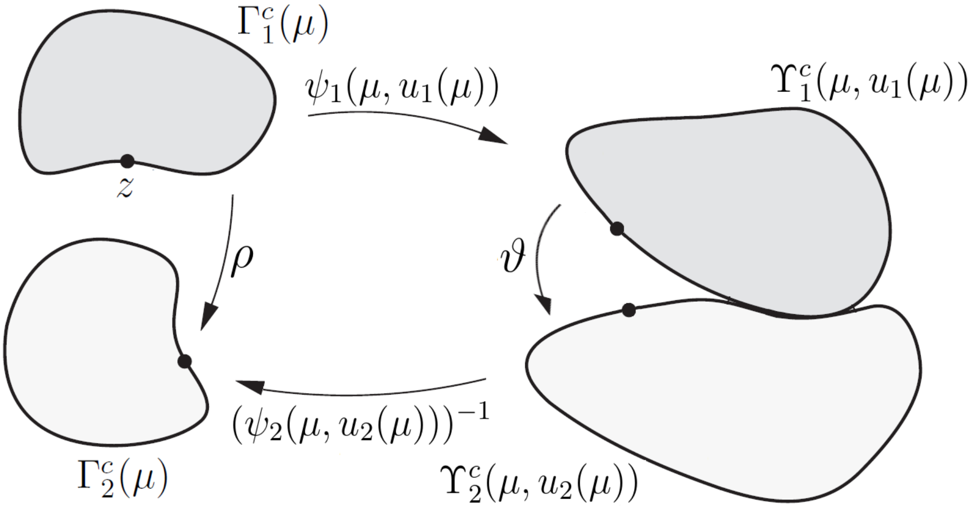

Figure 1: Generic two-body contact problem. For simplicity, the entire boundary is taken to be the potential contact boundary.

is well defined. For all $z \in \Upsilon_1^c(\mu, \widetilde{v}_1)$, $\vartheta(\mu, \widetilde{v})(z)$ is the orthogonal projection of z onto $\Upsilon_2^c(\mu, \widetilde{v}_2)$. The contact mapping $\vartheta(\mu, \widetilde{v})$ can be physically interpreted as the function relating every point on $\Upsilon_1^c(\mu, \widetilde{v}_1)$ to its potential contact point on $\Upsilon_2^c(\mu, \widetilde{v}_2)$. The contact mapping $\vartheta(\mu, \widetilde{v})$ depends on the displacement field $\widetilde{v}$ and is therefore unknown *a priori* for the solution $\widetilde{v} = \widetilde{u}(\mu)$. For all $\mu \in \mathcal{P}$ and all $\widetilde{v} \in \mathcal{V}(\mu)$, we define the mapping

$$\begin{cases} \rho(\mu, \widetilde{v}) : \Gamma_1^c(\mu) \to \Gamma_2^c(\mu) \\ \rho(\mu, \widetilde{v}) := (\psi_2(\mu, \widetilde{v}_2))^{-1} \circ \vartheta(\mu, \widetilde{v}) \circ \psi_1(\mu, \widetilde{v}_1), \end{cases} \tag{23}$$

and the vector field of outward normals on $\Upsilon_2^c(\mu, \widetilde{v}_2)$ such that

$$\bar{n}_2(\mu, \widetilde{v}_2) : \Upsilon_2^c(\mu, \widetilde{v}_2) \to \mathbb{R}^d. \tag{24}$$

It is also convenient to introduce the vector field

$$\begin{aligned} &n_2(\mu, \widetilde{v}) : \Gamma_1^c(\mu) \to \mathbb{R}^d \\ &n_2(\mu, \widetilde{v}) := \bar{n}_2(\mu, \widetilde{v}_2) \circ \vartheta(\mu, \widetilde{v}) \circ \psi_1(\mu, \widetilde{v}_1), \end{aligned} \tag{25}$$

which corresponds to the outward normal on $\Upsilon_2^c(\mu, \widetilde{v}_2)$ but defined at the corresponding point in $\Gamma_1^c(\mu)$ through the mapping $\vartheta(\mu, \widetilde{v}) \circ \psi_1(\mu, \widetilde{v}_1)$.

For an admissible solution $\widetilde{u}(\mu) = (\widetilde{u}_1(\mu), \widetilde{u}_2(\mu)) \in \mathcal{V}(\mu)$, the non-interpenetration condition reads: For all $z \in \Gamma_1^c(\mu)$,

$$\begin{aligned} \left(\widetilde{u}_1(\mu)(z) - \left(\widetilde{u}_2(\mu) \circ \rho(\mu, \widetilde{u}(\mu))\right)(z)\right) \cdot n_2(\mu, \widetilde{u}(\mu))(z) \\ \geqslant \left(\rho(\mu, \widetilde{u}(\mu))(z) - z\right) \cdot n_2(\mu, \widetilde{u}(\mu))(z). \end{aligned} \tag{26}$$

At this stage, we can define the displacement mapping $\widetilde{k} : \mathcal{P} \times \mathcal{V}(\mu) \times \mathcal{V}(\mu) \to \mathbb{R}$ and the gap mapping $\widetilde{g} : P \times \mathcal{V}(\mu) \to \mathbb{R}$ as

$$\widetilde{k}(\mu, \widetilde{w}; \widetilde{v})(z) := \left(\left(\widetilde{v}_2 \circ \rho(\mu, \widetilde{w})\right)(z) - \widetilde{v}_1(z)\right) \cdot n_2(\mu, \widetilde{w})(z), \tag{27}$$

and

$$\widetilde{g}(\mu, \widetilde{w})(z) := (z - \rho(\mu, \widetilde{w})(z)) \cdot n_2(\mu, \widetilde{w})(z), \tag{28}$$

for all $z \in \Gamma_1^c(\mu)$. The distinction between the arguments $\widetilde{v}$ and $\widetilde{w}$ in (27) is introduced so that $\widetilde{k}$ is linear with respect to $\widetilde{v}$. Hence, (26) can be recast as $\widetilde{k}(\mu, \widetilde{u}(\mu); \widetilde{u}(\mu)) \leqslant \widetilde{g}(\mu, \widetilde{u}(\mu))$, leading to the inequality constraint considered in (1). For all $\mu \in \mathcal{P}$, the admissible displacement $\widetilde{u}(\mu) \in \mathcal{V}(\mu)$ is then solution to

$$\begin{cases} \widetilde{u}(\mu) = \underset{\widetilde{v} \in \mathcal{V}(\mu)}{\operatorname{argmin}} \ \dfrac{1}{2}\widetilde{a}(\mu; \widetilde{v}, \widetilde{v}) - \widetilde{f}(\mu; \widetilde{v}) \\ \widetilde{k}(\mu, \widetilde{u}(\mu); \widetilde{u}(\mu)) \leqslant \widetilde{g}(\mu, \widetilde{u}(\mu)) \quad \text{a.e. on } \Gamma_1^c(\mu). \end{cases} \tag{29}$$

Remark 2 (Geometric interpretation)**.** *As proven in [22], Section 3.7.3, the constraint* (26) *is equivalent to*

$$\overline{\Omega}_1(\mu, \widetilde{u}_1(\mu)) \cap \overline{\Omega}_2(\mu, \widetilde{u}_2(\mu)) \subset \Upsilon_1^c(\mu, \widetilde{u}_1(\mu)) \cap \Upsilon_2^c(\mu, \widetilde{u}_2(\mu)), \tag{30}$$

where

$$\overline{\Omega}_i(\mu, \widetilde{u}_i(\mu)) := (Id + \widetilde{u}_i(\mu))(\overline{\Omega}_i(\mu)), \quad \forall i \in \{1, 2\}, \tag{31}$$

i.e. the intersection of the two deformed solids $\overline{\Omega}_1(\mu, \widetilde{u}_1(\mu))$ *and* $\overline{\Omega}_2(\mu, \widetilde{u}_2(\mu))$ *is necessarily a subset of their contact boundaries. Note that the indices* 1 *and* 2 *play symmetric roles in* (30)*.*

3.3 Reference domain

Let us now detail how the frictionless contact problem introduced in Sections 3.1-3.2 can be recast into the form (1) using a parameter-independent geometry. We assume that there exists a bi-Lipschitz diffeomorphism called geometric mapping $h(\mu)$ defined on a parameter-independent reference domain Ω such that

$$\begin{aligned} h(\mu) : \Omega &\to \Omega(\mu) \\ x &\mapsto \sum_{i=1}^{I} h_i(\mu)(x) \mathbf{1}_{\Omega_i}(x), \end{aligned} \tag{32}$$

where $\{\Omega_i\}_{i=1}^I$ is a partition of Ω. Using this geometric mapping, we introduce the reference Hilbert space

$$\mathcal{V} := H^1(\Omega; \mathbb{R}^d), \tag{33}$$

composed of functions defined on Ω such that $\mathcal{V}(\mu) := \mathcal{V} \star h(\mu)^{-1} := \{v \circ h(\mu)^{-1} \mid v \in \mathcal{V}\}$. For all $i \in \{1, \dots, I\}$, we set

$$\Omega_i(\mu) := h_i(\mu)(\Omega_i). \tag{34}$$

In what follows, we assume for simplicity that $I = 2$, which corresponds to the situation from Section 3 where there are two disjoint solids $\Omega_1(\mu)$ and $\Omega_2(\mu)$ that can come into contact. We fix the contact boundaries Γ_i^c, $i \in \{1, 2\}$, on the parameter-independent configuration Ω, and we define the parametric contact boundaries $\Gamma_i^c(\mu)$, $i \in \{1, 2\}$, as

$$\Gamma_i^c(\mu) := h_i(\mu)(\Gamma_i^c), \quad \forall i \in \{1, 2\}. \tag{35}$$

Note that $h_i(\mu)|_{\Gamma_i^c}$ defines a diffeomorphism from Γ_i^c to $\Gamma_i^c(\mu)$ for all $i \in \{1, 2\}$.

Let us now define the forms $a : \mathcal{P}\times\mathcal{V}\times\mathcal{V} \to \mathbb{R}$, $f : \mathcal{P}\times\mathcal{V} \to \mathbb{R}$, and the mappings $k : \mathcal{P}\times\mathcal{V}\times\mathcal{V} \to \mathbb{R}$ and $g : \mathcal{P} \times \mathcal{V} \to \mathbb{R}$ such that, for all $\mu \in \mathcal{P}$ and $v, w \in \mathcal{V}$,

$$
\begin{aligned}
a(\mu; v, w) &:= \tilde{a}\left(\mu; v \circ h(\mu)^{-1}, w \circ h(\mu)^{-1}\right), && (36)\\
f(\mu; w) &:= \tilde{f}\left(\mu; w \circ h(\mu)^{-1}\right), && (37)\\
k(\mu, w; v) &:= \tilde{k}\left(\mu, w \circ h(\mu)^{-1}; v \circ h(\mu)^{-1}\right)\left|\det\left(\mathrm{Jac}(h_1(\mu)_{|\Gamma_1^c})\right)\right|, && (38)\\
g(\mu, w) &:= \tilde{g}\left(\mu, w \circ h(\mu)^{-1}\right)\left|\det\left(\mathrm{Jac}(h_1(\mu)_{|\Gamma_1^c})\right)\right|, && (39)
\end{aligned}
$$

where $\det\left(\mathrm{Jac}(h_1(\mu)_{|\Gamma_1^c(\mu)})\right)$ refers to the determinant of the Jacobian matrix of $h_1(\mu)_{|\Gamma_1^c(\mu)}$. It is clear that for all $\mu \in \mathcal{P}$, finding $\tilde{u}(\mu) \in \mathcal{V}(\mu)$ solution to (29) is equivalent to finding $u(\mu) \in \mathcal{V}$ solution to

$$
\begin{cases}
u(\mu) = \underset{v\in\mathcal{V}}{\operatorname{argmin}}\ \dfrac{1}{2}a(\mu; v, v) - f(\mu; v) \\
k(\mu, u(\mu); u(\mu)) \leqslant g(\mu, u(\mu)) \quad \text{a.e. on } \Gamma_1^c,
\end{cases}
\tag{40}
$$

via the identity $\tilde{u}(\mu) = u(\mu) \circ h(\mu)^{-1}$. Problem (40) is of the same form as Problem (1) with $\Gamma^c := \Gamma_1^c$; moreover, the forms a, f and the mappings k, g satisfy the assumptions described in Section 2. The dual formulation of (40) is (5) with the Lagrangian defined in (6) on $\mathcal{V}\times\mathcal{W}^+$ with $\mathcal{W}^+ := L^2(\Gamma^c; \mathbb{R}_+)$. Note that in the context of contact mechanics, the constraint is expressed using the normals in the deformed configuration and not on the reference one.

Remark 3 (Use of Jacobian)**.** *The factor involving the Jacobian is not needed in* (38)-(39) *since the constraint is enforced pointwise in* (40)*. One also sees that the operation of mapping from* Ω *to* $\Omega(\mu)$ *commutes with the devising of the dual formulation. Indeed, letting* $\mathcal{W}^+(\mu) := L^2(\Gamma_1^c(\mu); \mathbb{R}_+)$*, the dual formulation on the parameter-dependent domain* $\Omega(\mu)$ *is to find* $(\tilde{u}(\mu), \tilde{\lambda}(\mu)) \in \mathcal{V}(\mu) \times \mathcal{W}^+(\mu)$ *such that*

$$
(\tilde{u}(\mu), \tilde{\lambda}(\mu)) = \arg \underset{\tilde{v}\in\mathcal{V}(\mu), \tilde{\eta}\in\mathcal{W}^+(\mu)}{\operatorname{minmax}} \widetilde{\mathcal{L}}(\mu)(\tilde{v}, \tilde{\eta}),
$$

where the Lagrangian $\widetilde{\mathcal{L}}(\mu) : \mathcal{V}(\mu) \times \mathcal{W}^+(\mu) \to \mathbb{R}$ *is defined as*

$$
\widetilde{\mathcal{L}}(\mu)(\tilde{v}, \tilde{\eta}) := \frac{1}{2}\tilde{a}(\mu; \tilde{v}, \tilde{v}) - \tilde{f}(\mu; \tilde{v}) + \left(\int_{\Gamma_1^c(\mu)} \tilde{k}(\mu, \tilde{v}; \tilde{v})\tilde{\eta} - \int_{\Gamma_1^c(\mu)} \tilde{g}(\mu, \tilde{v})\tilde{\eta}\right).
$$

Then the solutions to the dual formulations posed on Ω *and on* $\Omega(\mu)$ *are linked by the relations* $\tilde{u}(\mu) = u(\mu) \circ h(\mu)^{-1}$ *and* $\tilde{\lambda}(\mu) = \lambda(\mu) \circ h_1(\mu)^{-1}_{|\Gamma_1^c(\mu)}$.

4 The reduced-basis model

In this section, we return to the abstract setting of Section 2 and we derive a general RB formulation for the nonlinear minimization problem (1), and more precisely its algebraic saddle-point formulation (9).

4.1 Reduced basis spaces

Recall that $V_{\mathcal{N}}$ and $W_{\mathcal{R}}^+$ are the FEM discretizations of the Hilbert space $\mathcal{V}$ and the cone $\mathcal{W}^+$, respectively. In view of an accurate approximation of the solution manifold, we introduce the primal

RB subspace $\widehat{V}_N$ and the dual RB subcone $\widehat{W}_R^+$ that satisfy

$$\widehat{V}_N \subset V_{\mathcal{N}} \subset \mathcal{V} \quad \text{and} \quad \widehat{W}_R^+ \subset W_{\mathcal{R}}^+ \subset \mathcal{W}^+, \tag{41}$$

where the subscripts refer to the dimensions and are typically such that $N \ll \mathcal{N}$ and $R \ll \mathcal{R}$.

Let $(\theta_n)_{1\leqslant n\leqslant N}$ be a (orthonormal) basis of $\widehat{V}_N$ and let $(\xi_r)_{1\leqslant r\leqslant R}$ be generating vectors of the cone $\widehat{W}_R^+$, i.e., $\widehat{W}_R^+ = \mathrm{span}_+\{\xi_1, \ldots, \xi_R\}$. For all $\mu \in \mathcal{P}$, the primal RB solution $\widehat{u}(\mu) \in \widehat{V}_N$ and the dual RB solution (Lagrange multipliers) $\widehat{\lambda}(\mu) \in \widehat{W}_R^+$ that approximate the HF solution $(u_{\mathcal{N}}(\mu), \lambda_{\mathcal{R}}(\mu)) \in V_{\mathcal{N}} \times W_{\mathcal{R}}^+$ are decomposed as

$$\widehat{u}(\mu) = \sum_{n=1}^{N} \widehat{u}_n(\mu)\theta_n \quad \text{and} \quad \widehat{\lambda}(\mu) = \sum_{r=1}^{R} \widehat{\lambda}_r(\mu)\xi_r, \tag{42}$$

with real numbers $\widehat{u}_n(\mu)$ for all $n \in \{1, \ldots, N\}$ and non-negative real numbers $\widehat{\lambda}_r(\mu)$ for all $r \in \{1, \ldots, R\}$. Introducing the component vectors $\widehat{\mathbf{u}}(\mu) := (\widehat{u}_n(\mu))_{1\leqslant n\leqslant N}$ and $\widehat{\boldsymbol{\lambda}}(\mu) := (\widehat{\lambda}_r(\mu))_{1\leqslant r\leqslant R}$, for all $\mu \in \mathcal{P}$, the RB formulation of (9) reads: Find $(\widehat{\mathbf{u}}(\mu), \widehat{\boldsymbol{\lambda}}(\mu)) \in \mathbb{R}^N \times \mathbb{R}_+^R$ such that

$$(\widehat{\mathbf{u}}(\mu), \widehat{\boldsymbol{\lambda}}(\mu)) \in \arg \min_{\widehat{\mathbf{v}}\in\mathbb{R}^N,\widehat{\boldsymbol{\eta}}\in\mathbb{R}_+^R}\max \frac{1}{2}\widehat{\mathbf{v}}^T\widehat{\mathbf{A}}(\mu)\widehat{\mathbf{v}} - \widehat{\mathbf{v}}^T\widehat{\mathbf{f}}(\mu) + \widehat{\boldsymbol{\eta}}^T\big(\widehat{\mathbf{K}}(\mu, \widehat{\mathbf{v}})\widehat{\mathbf{v}} - \widehat{\mathbf{g}}(\mu, \widehat{\mathbf{v}})\big), \tag{43}$$

with the matrices $\widehat{\mathbf{A}}(\mu) \in \mathbb{R}^{N\times N}$ and $\widehat{\mathbf{K}}(\mu, \widehat{\mathbf{v}}) \in \mathbb{R}^{R\times N}$ such that

$$\widehat{\mathbf{A}}(\mu)_{pn} = a(\mu; \theta_n, \theta_p), \tag{44a}$$

$$\widehat{\mathbf{K}}(\mu, \widehat{\mathbf{v}})_{rn} = \int_{\Gamma^c} k\bigg(\mu, \sum_{i=1}^{N} \widehat{v}_i\theta_i; \theta_n\bigg)\xi_r, \tag{44b}$$

and the vectors $\widehat{\mathbf{f}}(\mu) \in \mathbb{R}^N$ and $\widehat{\mathbf{g}}(\mu, \widehat{\mathbf{v}}) \in \mathbb{R}^R$ such that

$$\widehat{\mathbf{f}}(\mu)_p = f(\mu; \theta_p), \tag{45a}$$

$$\widehat{\mathbf{g}}(\mu, \widehat{\mathbf{v}})_r = \int_{\Gamma^c} g\left(\mu, \sum_{i=1}^{N} \widehat{v}_i\theta_i\right)\xi_r. \tag{45b}$$

4.2 Separation of the elastic energy

We assume the existence of two integers J^a and J^f and of continuous bilinear forms $a_j : \mathcal{V} \times \mathcal{V} \to \mathbb{R}$, with $1 \leqslant j \leqslant J^a$, and continuous linear forms $f_j : \mathcal{V} \to \mathbb{R}$, with $1 \leqslant j \leqslant J^f$, such that the bilinear form $a(\mu; \cdot, \cdot)$ and the linear form $f(\mu; \cdot)$ can be affinely decomposed as follows: For all $v, w \in \mathcal{V}$,

$$a(\mu; v, w) = \sum_{j=1}^{J^a} \alpha_j^a(\mu)a_j(v, w), \text{ and } f(\mu; w) = \sum_{j=1}^{J^f} \alpha_j^f(\mu)f_j(w), \tag{46}$$

for some functions $\alpha_j^a : \mathcal{P} \to \mathbb{R}$, for all $1 \leqslant j \leqslant J^a$, and $\alpha_j^f : \mathcal{P} \to \mathbb{R}$, for all $1 \leqslant j \leqslant J^f$.

The separated representations in (46) hold true in the setting of contact mechanics considered in Section 3 under some reasonable assumptions. Let us exemplify the case of the load $f(\mu; w)$. For all

$w \in \mathcal{V}$, using the definition of the geometric mapping $h(\mu)$ in (32), we have

$$\begin{aligned} f(\mu; w) &= \int_{\Omega(\mu)} \ell(\mu) \cdot w \circ h(\mu)^{-1} = \sum_{i=1}^{2} \int_{\Omega_i(\mu)} \ell(\mu) \cdot w \circ h_i(\mu)^{-1} \\ &= \sum_{i=1}^{2} \int_{\Omega_i} \ell(\mu)(h_i(\mu)(x)) \cdot w(x) \left|\det\left(\mathrm{Jac}(h_i(\mu))(x)\right)\right| \, dx, \end{aligned} \tag{47}$$

where the notation $\det(\mathrm{Jac}(h_i(\mu)))$ refers to the determinant of the Jacobian matrix of the geometric mapping $h_i(\mu)$. Let us assume that the load function $\ell(\mu)$ is space-independent and that the geometric mappings $h_i(\mu)$, $i \in \{1, 2\}$, are affine, i.e. that there exists $M_i(\mu) \in \mathbb{R}^{d\times d}$ and $b_i(\mu) \in \mathbb{R}^d$ such that for all $x \in \Omega_i$, $h_i(\mu)(x) = M_i(\mu)x + b_i(\mu)$, for all $\mu \in \mathcal{P}$. These assumptions are satisfied in the numerical cases presented in Section 6. Then, we obtain, for all $v \in \mathcal{V}$,

$$f(\mu; w) = \sum_{i=1}^{2} \int_{\Omega_i} \ell(\mu) \cdot w(x) \left|\det M_i(\mu)\right| \, dx = \sum_{i=1}^{2} \left|\det M_i(\mu)\right| \ell(\mu) \cdot \int_{\Omega_i} w(x)\, dx. \tag{48}$$

Let $(e_k)_{1\leqslant k\leqslant d}$ be the canonical basis of $\mathbb{R}^d$, and let $\ell_k(\mu) := e_k \cdot \ell(\mu)$ for all $1 \leqslant k \leqslant d$. Consequently, in (46), we have $J^f = 2d$, and for all $1 \leqslant j \leqslant 2d$, $\alpha_j^f(\mu) := h_i(\mu)\ell_k(\mu)$ and $f_j(w) := \int_{\Omega_i} e_k \cdot w(x)\, dx$, where $k := \lfloor (j-1)/2 \rfloor + 1$ and $i := j - 2(k-1)$ (the notation $\lfloor\cdot\rfloor$ standing for the integer part). Similarly, under the same assumption on $h(\mu)$, a separated representation of $a(\mu; \cdot, \cdot)$ is available.

In the general case where the dependencies on μ are non-affine, one typically resorts to the EIM [16, 17] in order to build approximate separated representations of $a(\mu; \cdot, \cdot)$ and $f(\mu; \cdot)$.

The separated expressions (46) imply that the matrix $\widehat{\mathbf{A}}(\mu)$ defined in (44a) and the vector $\widehat{\mathbf{f}}(\mu)$ defined in (45a) can be affinely decomposed under the form

$$\left(\widehat{\mathbf{A}}(\mu)\right)_{np} = \sum_{j=1}^{J^a} \alpha_j^a(\mu)\widehat{\mathbf{A}}_{j,np} \text{ and } \left(\widehat{\mathbf{f}}(\mu)\right)_{p} = \sum_{j=1}^{J^f} \alpha_j^f(\mu)\widehat{\mathbf{f}}_{j,p}, \ \forall 1 \leqslant n, p \leqslant N, \tag{49}$$

where $\widehat{\mathbf{A}}_{j,np} := a_j(\theta_p, \theta_n)$ and $\widehat{\mathbf{f}}_{j,p} := f_j(\theta_p)$. The key point is that the dependencies on μ and n, p are separated in (49). Therefore, the matrix $\widehat{\mathbf{A}}_{j,np}$ and the vector $\widehat{\mathbf{f}}_{j,p}$ are offline-computable, and all that remains to be performed during the online stage is the assembly of the matrix $\widehat{\mathbf{A}}(\mu)$ and the vector $\widehat{\mathbf{f}}(\mu)$ using (49) for each new parameter value $\mu \in \mathcal{P}$.

4.3 Separation of the constraint

The remaining bottleneck is the computation of the matrix $\widehat{\mathbf{K}}(\mu, \hat{\mathbf{v}})$ and the vector $\widehat{\mathbf{g}}(\mu, \hat{\mathbf{v}})$ in (44b) and (45b) respectively. Indeed, these computations require parameter-dependent reconstructions using the FEM basis functions $(\theta_n)_{1\leqslant n\leqslant N}$ in order to compute the integrals over Γ^c. The key idea is to search for approximations κ_{M^k} and γ_{M^g} of the nonlinear mappings $\kappa : \mathcal{P} \times \{1, \ldots, \mathcal{N}\} \times \Gamma^c \to \mathbb{R}$ and $\gamma : \mathcal{P} \times \Gamma^c \to \mathbb{R}$ defined such that

$$\kappa(\mu, n, x) := k(\mu, u(\mu); \phi_n)(x) \quad \text{and} \quad \gamma(\mu, x) := g(\mu, u(\mu))(x). \tag{50}$$

Our goal in building these approximations is to separate the dependence on μ from the dependence on the other variables. More precisely, for some integers $M^k, M^g \geqslant 1$, we look for (accurate) approximations $\kappa_{M^k} : \mathcal{P} \times \{1, \ldots, \mathcal{N}\} \times \Gamma^c \to \mathbb{R}$ of κ and $\gamma_{M^g} : \mathcal{P} \times \Gamma^c \to \mathbb{R}$ of γ in the separated form

$$\kappa_{M^k}(\mu,n,x) := \sum_{j=1}^{M^k} \varphi_j^\kappa(\mu) q_j^\kappa(n,x), \qquad \gamma_{M^g}(\mu,x) := \sum_{j=1}^{M^g} \varphi_j^\gamma(\mu) q_j^\gamma(x), \tag{51}$$

where M^k (resp. M^g) is called the rank of the approximation and φ_j^κ (resp. φ_j^γ) are real-valued functions of the parameter μ that are found by interpolation. For κ_{M^k}, we interpolate over a set of M^k pairs $\{(n_1^\kappa, x_1^\kappa), \ldots, (n_{M^k}^\kappa, x_{M^k}^\kappa)\}$ in $\{1,\ldots,\mathcal{N}\} \times \Gamma^c$, whereas for γ_{M^g}, we interpolate over a set of M^g points $\{x_1^\gamma, \ldots, x_{M^g}^\gamma\}$ in Γ^c. The interpolation is performed using the EIM [16] and leads to the vector $\widehat{\boldsymbol{\kappa}}(\mu, \widehat{\mathbf{v}}) \in \mathbb{R}^{M^k}$, the matrix $\mathbf{B}^\kappa \in \mathbb{R}^{M^k \times M^k}$, the vector $\widehat{\boldsymbol{\gamma}}(\mu, \widehat{\mathbf{v}}) \in \mathbb{R}^{M^g}$ and the matrix $\mathbf{B}^\gamma \in \mathbb{R}^{M^g \times M^g}$ defined as follows:

$$\begin{cases} \widehat{\boldsymbol{\kappa}}(\mu, \widehat{\mathbf{v}})_i := k(\mu, \widehat{v}; \phi_{n_i}^\kappa)(x_i^\kappa), \\ \mathbf{B}_{ij}^\kappa = q_j^\kappa(n_i^\kappa, x_i^\kappa), \\ \widehat{\boldsymbol{\gamma}}(\mu, \widehat{\mathbf{v}})_i := g(\mu, \widehat{v})(x_i^\gamma), \\ \mathbf{B}_{ij}^\gamma = q_j^\gamma(x_i^\gamma). \end{cases} \tag{52}$$

Note that the EIM guarantees the invertibility of the matrices $\mathbf{B}^\kappa$ and $\mathbf{B}^\gamma$. After the approximation resulting from the separation of the constraint, the problem (43) becomes (we keep the same notation for its solution)

$$\begin{aligned} (\widehat{\mathbf{u}}(\mu), \widehat{\boldsymbol{\lambda}}(\mu)) \in \arg \min_{\widehat{\mathbf{v}} \in \mathbb{R}^N, \widehat{\boldsymbol{\eta}} \in \mathbb{R}_+^R} \max \Big\{ & \frac{1}{2} \widehat{\mathbf{v}}^T \widehat{\mathbf{A}}(\mu) \widehat{\mathbf{v}} - \widehat{\mathbf{v}}^T \widehat{\mathbf{f}}(\mu) \\ & + \widehat{\boldsymbol{\eta}}^T \big(\mathbf{D}^\kappa(\mu, \widehat{\mathbf{v}}) \widehat{\mathbf{v}} - \mathbf{D}^\gamma(\widehat{\mathbf{v}}) \widehat{\boldsymbol{\gamma}}(\mu, \widehat{\mathbf{v}}) \big) \Big\}, \end{aligned} \tag{53}$$

with the matrices

$$\mathbf{D}^\kappa(\mu, \widehat{\mathbf{v}}) := \sum_{j=1}^{M^k} \mathbf{C}_j^\kappa ((\mathbf{B}^\kappa)^{-1} \widehat{\boldsymbol{\kappa}}(\mu; \widehat{\mathbf{v}}))_j \quad \text{and} \quad \mathbf{D}^\gamma := \mathbf{C}^\gamma (\mathbf{B}^\gamma)^{-1}, \tag{54}$$

where $\mathbf{C}_j^\kappa \in \mathbb{R}^{R \times N}$ and $\mathbf{C}^\gamma \in \mathbb{R}^{R \times M^g}$ are given by

$$\mathbf{C}_j^\kappa := \left(\sum_{i=1}^{\mathcal{N}} \int_{\Gamma^c} \theta_{n,i} q_j^\kappa(i, \cdot) \xi_r \right)_{rn} \quad \text{and} \quad \mathbf{C}^\gamma := \left(\int_{\Gamma^c} q_{j'}^\gamma \xi_r \right)_{pj'}, \tag{55}$$

for all $j \in \{1, \ldots, M^\kappa\}$, all $r \in \{1, \ldots, R\}$, all $n \in \{1, \ldots, N\}$, and all $j' \in \{1, \ldots, M^\gamma\}$.

The overall computational procedure can now be split into two stages:

(i) An offline stage where one precomputes on the one hand the RB subspace $\widehat{V}_N$ and the RB subcone $\widehat{W}_R^+$ leading to the vectors $\{\widehat{\mathbf{f}}_r\}_{1 \leqslant r \leqslant J^f}$ in $\mathbb{R}^N$ and the matrices $\{\widehat{\mathbf{A}}_r\}_{1 \leqslant r \leqslant J^a}$ in $\mathbb{R}^{N \times N}$, and on the other hand the EIM pairs $\{(n_i^\kappa, x_i^\kappa)\}_{1 \leqslant i \leqslant M^k}$, the EIM points $\{x_i^\gamma\}_{1 \leqslant i \leqslant M^g}$, the EIM functions $\{q_j^\kappa\}_{1 \leqslant j \leqslant M^k}$, and the EIM functions $\{q_j^\gamma\}_{1 \leqslant j \leqslant M^g}$, leading to the matrices $\mathbf{B}^\kappa \in \mathbb{R}^{M^k \times M^k}$, $\mathbf{B}^\gamma \in \mathbb{R}^{M^g \times M^g}$, $\{\mathbf{C}_j^\kappa\}_{1 \leqslant j \leqslant M^k} \subset \mathbb{R}^{R \times N}$, and $\mathbf{C}^\gamma \in \mathbb{R}^{R \times M^g}$. The offline stage is discussed in more detail in Section 5.

(ii) An online stage to be performed each time one wishes to compute a new solution for a parameter $\mu \in \mathcal{P}$. All that remains to be performed is to assemble the vector $\widehat{\mathbf{f}}(\mu) \in \mathbb{R}^N$ and the matrix $\widehat{\mathbf{A}}(\mu) \in \mathbb{R}^{N \times N}$ using (49), to compute the vectors $\widehat{\boldsymbol{\kappa}}(\mu, \widehat{\mathbf{v}}) \in \mathbb{R}^{M^k}$ and $\widehat{\boldsymbol{\gamma}}(\mu, \widehat{\mathbf{v}}) \in \mathbb{R}^{M^g}$ defined in (52), to assemble the matrix $\mathbf{D}^\kappa(\mu, \widehat{\mathbf{v}})$ defined in (54), and to solve the reduced saddle-point problem (53). The online stage is summarized in Algorithm 1.

Algorithm 1 Online stage

```
Input : $\mu$, $\{\widehat{\mathbf{f}}_j\}_{1\leqslant j\leqslant J^f}$, $\{\widehat{\mathbf{A}}_j\}_{1\leqslant j\leqslant J^a}$, $\{(n_i^\kappa, x_i^\kappa)\}_{1\leqslant i\leqslant M^k}$, $\{x_i^\gamma\}_{1\leqslant i\leqslant M^g}$, $\{q_j^\kappa\}_{1\leqslant j\leqslant M^k}$, $\{q_j^\gamma\}_{1\leqslant j\leqslant M^g}$, $\mathbf{B}^\kappa$, $\{\mathbf{C}_j^\kappa\}_{1\leqslant j\leqslant M^k}$ and $\mathbf{D}^\gamma$.
Assemble the vector $\widehat{\mathbf{f}}(\mu)$ and the matrix $\widehat{\mathbf{A}}(\mu)$ using (49)
Compute $\widehat{\boldsymbol{\kappa}}(\mu, \widehat{\mathbf{v}})$ and $\widehat{\boldsymbol{\gamma}}(\mu, \widehat{\mathbf{v}})$ using (52)
Compute $\mathbf{D}^\kappa(\mu)$ using $\widehat{\boldsymbol{\kappa}}(\mu, \widehat{\mathbf{v}})$ and (54)
Solve the reduced saddle-point problem (53) to obtain $\widehat{\mathbf{u}}(\mu)$ and $\widehat{\boldsymbol{\lambda}}(\mu)$
Output : $\widehat{\mathbf{u}}(\mu)$ and $\widehat{\boldsymbol{\lambda}}(\mu)$
```

Remark 4 (EIM matrices)**.** *The computations in Algorithm 1 only require the knowledge of the matrix* $(\mathbf{B}^\kappa)^{-1}$*. In order to optimize the computational costs,* $\mathbf{B}^\kappa$ *is inverted during the offline stage. The matrix* $\mathbf{B}^\gamma$ *is also inverted when computing the matrix* $\mathbf{D}^\gamma$ *during the offline stage (see* (54)*). Since these matrices may be ill-conditioned, whenever an inversion is required, a linear system solve is recommended, along with the storage of the LU decomposition to be used whenever a vector multiplication by the EIM matrix is needed during the online stage.*

Remark 5 (EIMs on k and g)**.** *Owing to the quasi-linear structure of the inequality constraint, the reduced problem* (53) *can be solved using the Kačanov method. At first glance, the influence of this solution choice is that we have to perform the EIM twice since the mappings* k *and* g *are separated one at a time. Were we to use a Newton method by considering the one-term constraint* $\zeta(\mu, u(\mu)) \leqslant 0$ *(see* (2)*), we would only perform a single EIM. However, an additional EIM would be needed in the Newton method in order to compute the Jacobian preconditioning matrix. Thus, both methods (Kačanov or Newton) lead to two distinct EIMs and the storage cost is essentially the same.*

5 The offline stage

There are two main tasks to be performed during the offline stage:

(T_1) Build the rank-M^k and the rank-M^g EIM approximations in (51);

(T_2) Explore the solution manifold in order to construct the linear subspace $\widehat{V}_N \subset V_\mathcal{N}$ of dimension N and the subcone $\widehat{W}_R^+ \subset W_\mathcal{R}^+$ of dimension R.

Tasks (T_1) and (T_2) can be performed independently and in whatever order. Since Task (T_1) can be considered to be standard, we only discuss Task (T_2), i.e., the construction of the sets of primal and dual RB functions with cardinalities N and R respectively. First, as usual in RB methods, the solution manifold is explored by considering a training set for the parameter values. For simplicity, one can consider the same training set $\mathcal{P}^{\mathrm{tr}}$ as for the EIM approximations. This way, one only explores the collection of snapshots $\mathcal{S}_{\mathrm{PRI}} = \{u(\mu)\}_{\mu\in\mathcal{P}^{\mathrm{tr}}}$ and $\mathcal{S}_{\mathrm{DU}} = \{\lambda(\mu)\}_{\mu\in\mathcal{P}^{\mathrm{tr}}}$ in the primal and dual solution manifolds respectively. For this exploration to be informative, the training set $\mathcal{P}^{\mathrm{tr}}$ has to be chosen large enough. In the present setting where HF solutions are to be computed for all the parameters in $\mathcal{P}^{\mathrm{tr}}$ when constructing the EIM approximations, the present choice is to compress these computations by means of a Proper Orthogonal Decomposition (POD) [23, 24, 25] to define the primal RB subspace $\widehat{V}_N$. One can also resort to the strong greedy algorithm using the true projection error. Choosing between the POD and the strong greedy depends on whether one aims at an L^2-error or H^1-error (POD) or an L^∞-error (strong greedy) over the parameter domain.

Bearing in mind that the dual RB cone $\widehat{W}_R^+$ is meant to represent the set of Lagrange multipliers, its spanning vectors should all have non-negative components. Consequently, the POD is not appropriate to build $\widehat{W}_R^+$. If the training set has a moderate size, one could keep all the Lagrange multiplier snapshots, especially if they have been computed via *a posteriori* error estimation. In [4], it is suggested to use the Non-negative Matrix Factorization (NMF) algorithm [5] whenever the number of training snapshots is relatively large, for instance in the case of a time-dependent problem. For a set of snapshots $\mathcal{S}_{\mathrm{DU}}$ and an integer R, the procedure $\mathrm{NMF}(\mathcal{S}_{\mathrm{DU}}, R)$ returns R vectors $(w_1, \ldots, w_R)$ with non-negative components (the procedure is briefly recalled in Section A). ~~Nonetheless, the resulting dual RB cone can be less accurate than the primal RB space.~~ Moreover, the user does not specify an error tolerance but only the cardinality of the family of vectors generating the dual RB cone. In practice, it is often difficult to anticipate how well the dual RB cone approximates the HF cone only from its cardinality (see the numerical results in Section 6 for illustrations).

Here, we suggest to build a dual hierarchical RB cone from the Lagrange multiplier snapshots computed offline by means of a so-called the Cone-Projected Greedy (CPG) algorithm. In the spirit of weak greedy algorithms, the idea is to order the snapshots depending on their relevance to represent the entire set of snapshots. The algorithm reads as follows: First, we choose $\mu_1 \in \mathcal{P}^{\mathrm{tr}}$ such that

$$\mu_1 \in \underset{\mu \in \mathcal{P}^{\mathrm{tr}}}{\operatorname{argmax}} \, \|\lambda(\mu)\|_\Lambda. \tag{56}$$

The most natural choice for the norm on the Lagrange multipliers is $\|\cdot\|_\Lambda = \|\cdot\|_{L^2(\Gamma^c)}$. However, at the discrete level, one can also consider the choice $\|\cdot\|_\Lambda = \|\cdot\|_{\ell^\infty(\Gamma^{c,\mathrm{tr}})}$, where $\Gamma^{c,\mathrm{tr}} \subsetneq \Gamma^c$ is a discrete subset of Γ^c.

Afterwards, at each iteration $n \geqslant 2$, we define the convex cone $\widehat{K}_{n-1}^+ = \mathrm{span}_+\{\lambda(\mu_1), \ldots, \lambda(\mu_{n-1})\}$ and select a new parameter value $\mu_n \in \mathcal{P}^{\mathrm{tr}}$ using the criterion

$$\mu_n \in \underset{\mu \in \mathcal{P}^{\mathrm{tr}}}{\operatorname{argmax}} \, \|\lambda(\mu) - \Pi_{\widehat{K}_{n-1}^+}(\lambda(\mu))\|_\Lambda, \tag{57}$$

where $\Pi_{\widehat{K}_{n-1}^+}$ is the L^2-orthogonal projector onto the convex cone $\widehat{K}_{n-1}^+$. At each iteration, we check whether or not the stopping criterion

$$\max_{\mu \in \mathcal{P}^{\mathrm{tr}}} \|\lambda(\mu) - \Pi_{\widehat{K}_{n-1}^+}(\lambda(\mu))\|_\Lambda \leqslant \epsilon_{\mathrm{DU}}, \tag{58}$$

is fulfilled. One can also consider a relative error criterion instead of an absolute one by dividing the left-hand side of (58) by $\|\lambda(\mu)\|_\Lambda$. The CPG algorithm is summarized in Algorithm 2. The main difference between the CPG and the angle-greedy algorithm from [13] is that the latter selects the parameter that maximizes the error of a linear projection. In other words, in the angle-greedy algorithm, line 5 of Algorithm 2 is replaced by $\mu_n \in \operatorname{argmax}_{\mu \in \mathcal{P}^{\mathrm{tr}}} \|\lambda(\mu) - \Pi_{\widehat{W}_{n-1}}(\lambda(\mu))\|_\Lambda$, where $\widehat{W}_{n-1} = \mathrm{span}\{\lambda_1(\mu), \ldots, \lambda_{n-1}(\mu)\}$ is a linear space. Hence, the stopping criterion in the angle-greedy algorithm does not necessarily reflect the accuracy obtained for the training set, whereas the stopping criterion for the CPG represents an accuracy that is effectively satisfied for the training set when approximating its elements by positive projections on the RB dual cone. Differences between the two algorithms are expected to appear when some Lagrange multipliers are (or are close to being) collinear. An elementary illustration is presented in Remark 6. However, in practice, the angle-greedy algorithm turns out to be efficient for the test cases considered in [13], and it is also the case for the test cases considered herein. When it comes to computational cost, the angle-greedy algorithm is somewhat faster than the CPG algorithm since the former performs linear projections whereas the latter requires positive projections. The availability of an efficient, off-the-shelf library to perform positive projections (see [26]) is a further motivation for using the CPG. For instance, for the test case discussed in Section 6.3 below, the execution time of the CPG is about ten times that of the angle-greedy algorithm, but it represents less than 1% of the total cost, the constrained HF computations being the most expensive part of the offline stage.

Remark 6 (Comparison in a simplified setting). *Consider an angle* $\zeta \in]0, \pi/6]$ *and the training set of Lagrange multipliers* $\mathcal{L} = \{e_1, e_2, e_3, e_4\}$ *composed of the following column vectors in* $\mathbb{R}^3$*:*

$$e_1 = \begin{pmatrix} \cos(\zeta) \\ \sin(\zeta) \\ 0 \end{pmatrix}, \quad e_2 = 2\begin{pmatrix} \cos(2\zeta) \\ \sin(2\zeta) \\ 0 \end{pmatrix}, \quad e_3 = \frac{3}{2}\begin{pmatrix} \cos(3\zeta) \\ \sin(3\zeta) \\ 0 \end{pmatrix}, \quad e_4 = \begin{pmatrix} \cos(2\zeta) \\ \sin(2\zeta) \\ \sin(\zeta/2) \end{pmatrix}. \tag{59}$$

Consider the cone $\widehat{K}_2^+ = \mathrm{span}_+\{e_2, e_3\}$*. Then the CPG selects* e_1 *as the next vector since it is the most distant to the cone, whereas the angle-greedy criterion selects* e_4 *which is the most distant to the plane* $\mathrm{span}\{e_2, e_3\}$*. The difference in the selection between the CPG and the angle-greedy algorithms has been triggered here by the fact that* e_1 *is in* $\mathrm{span}\{e_2, e_3\}$*.*

Algorithm 2 Cone-Projected Greedy (CPG) algorithm

```
Input : $\mathcal{P}^{\mathrm{tr}}$ and $\epsilon_{\mathrm{DU}} > 0$
Compute $\mathcal{S}_{\mathrm{DU}} := \{\lambda(\mu)\}_{\mu\in\mathcal{P}^{\mathrm{tr}}}$        # HF solutions
Set $\widehat{K}_0^+ := \{0\}$
Set $n := 1$ and $r_1 := 2\epsilon_{\mathrm{DU}}$
while ($r_n > \epsilon_{\mathrm{DU}}$) do
    Search $\mu_n \in \operatorname*{argmax}_{\mu\in\mathcal{P}^{\mathrm{tr}}} \|\lambda(\mu) - \Pi_{\widehat{K}_{n-1}^+}(\lambda(\mu))\|_\Lambda$
    Set $\widehat{K}_n^+ := \mathrm{span}_+\{\lambda(\mu_1), \dots, \lambda(\mu_n)\}$
    Set $n := n + 1$
    Set $r_n := \max_{\mu\in\mathcal{P}^{\mathrm{tr}}} \|\lambda(\mu) - \Pi_{\widehat{K}_{n-1}^+}(\lambda(\mu))\|_\Lambda$
end while
Set $R := n - 1$
Output : $\widehat{W}_R^+ := \widehat{K}_R^+$.
```

Remark 7 (Elementary compression). *Additional computational savings can be achieved by suppressing the constraints that are never saturated for any of the parameters in the training set* $\mathcal{P}^{\mathrm{tr}}$ *but were initially introduced in the HF model. In practice, one can reduce the dimensions of the matrix* $\mathbf{K}(\mu, \mathbf{u}(\mu))$ *and the vector* $\mathbf{g}(\mu, \mathbf{u}(\mu))$ *appearing in (9) by removing the lines and columns of* $\mathbf{K}(\mu, \mathbf{u}(\mu))$ *and the components of* $\mathbf{g}(\mu, \mathbf{u}(\mu))$ *that always vanish no matter the value of the parameter* $\mu \in \mathcal{P}^{\mathrm{tr}}$*.*

6 Numerical results

In this section, we illustrate the above developments by two numerical examples related to elastic frictionless contact in a two-dimensional framework. The goal is to illustrate the computational performance of the proposed method. We first present two different methodologies to address the discretization of the constraint. Hence, Section 6.1 does not deal with model reduction and the reader familiar with the material can skip it. The first example is the contact problem between two half-disks introduced by Hertz in [18], whereas the second investigates a contact problem between a ring and a block as described in [19]. The HF computations use a combination of `Freefem++` [27] and `Python`, whereas the reduced-order modeling algorithms have been developed in `Python` using the convex optimization package `cvxopt` [26].

6.1 Discretization of the HF problem

Continuous piecewise affine finite elements are used to discretize the displacement field on triangular meshes of Ω_1 and Ω_2. We consider two different strategies for discretizing the constraint in the HF saddle-point problem (9); namely, a collocation method and the so-called Local Average Contact method (LAC) introduced in [28]. The collocation method amounts to node-to-segment non-interpenetration constraints in 2D (or to the equivalent node-to-face constraints in 3D). However, in many contexts, this method can produce dual solutions with oscillations thereby degrading the accuracy of the computations. The LAC method was designed to overcome the oscillation phenomenon. The price to pay is that the constraint is expressed in a somewhat less local form.

6.1.1 The collocation method

The collocation method expresses the non-interpenetration constraints at given collocation nodes. We choose these nodes, say $\{z_r\}_{1\leqslant r\leqslant\mathcal{R}}$, to be the boundary vertices of the mesh from Ω_1 located on $\Gamma^c = \Gamma_1^c$ (other choices are possible). Thus, the non-interpenetration constraints read

$$k(\mu, u_{\mathcal{N}}(\mu); u_{\mathcal{N}}(\mu))(z_r) \leqslant g(\mu, u_{\mathcal{N}}(\mu))(z_r), \quad \forall r \in \{1,\dots,\mathcal{R}\}. \tag{60}$$

The conditions in (60) can be interpreted as

$$\int_{\Gamma^c} k(\mu, u_{\mathcal{N}}(\mu); u_{\mathcal{N}}(\mu))\psi_r \leqslant \int_{\Gamma^c} g(\mu, u_{\mathcal{N}}(\mu))\psi_r, \quad \forall r \in \{1,\dots,\mathcal{R}\}, \tag{61}$$

where $\{\psi_r\}_{1\leqslant r\leqslant\mathcal{R}}$ are $\mathbb{P}_0$ basis functions with support centered on the collocation nodes, provided a one-node quadrature at the collocation nodes is used to approximate the integrals in (61).

6.1.2 The LAC method

In the LAC method, the admissible displacements satisfy the average non-interpenetration conditions

$$\int_{\Gamma^c} k(\mu, u_{\mathcal{N}}(\mu); u_{\mathcal{N}}(\mu))\psi_r \leqslant \int_{\Gamma^c} g(\mu, u_{\mathcal{N}}(\mu))\psi_r, \quad \forall r \in \{1,\dots,\mathcal{R}\}, \tag{62}$$

where $\{\psi_r\}_{1\leqslant r\leqslant\mathcal{R}}$ are $\mathbb{P}_0$ basis functions defined on Γ^c and supported on non-overlapping macro-segments $I^r \subset \Gamma^c$. The sole requirement on the macro-segments I^r is that each one contains at least one internal degree of freedom for the displacement. For instance, for a polynomial degree $k = 1$ of the primal HF space, the macro-segments comprise two adjacent segments that are boundary sides on Γ^c of the mesh from Ω_1. In other words, on a fixed mesh, there are two times more basis functions to enforce the constraints in the collocation method than in the LAC method. The integrals in (62) are approximated using Simpson's rule on I^r. Since the midpoint of a macro-segment I^r is also a boundary vertex of the mesh from Ω_1, this means that the integrals in (62) are evaluated only at these boundary vertices.

6.2 Half-disks of Hertz

Consider a two-dimensional setting based on two half-disks, where the upper one is denoted Ω_1 and the lower one Ω_2, see Figure 2. The radii of the disks are denoted R_1 and R_2, respectively, and the initial gap between the disks is $\gamma_0 = 0.1$m. We always set $R_1 = 1$m, whereas the value of R_2 depends on the test case. The materials of both half-disks are identical and correspond to a Young modulus $E = 15$Pa and a Poisson coefficient $\nu = 0.35$. HF solutions are computed using a finite element subspace defined on a mesh of Ω and consisting of continuous, piecewise affine functions. The potential contact zone is the circular part of the boundary of both disks. For a mesh with 675 nodes, Γ^c contains 51 nodes. Consequently, the problem has $\mathcal{N} = 1350$ degrees of freedom and $\mathcal{R} = 51$ Lagrange multipliers when using the collocation method and $\mathcal{R} = 25$ Lagrange multipliers when using the LAC method.

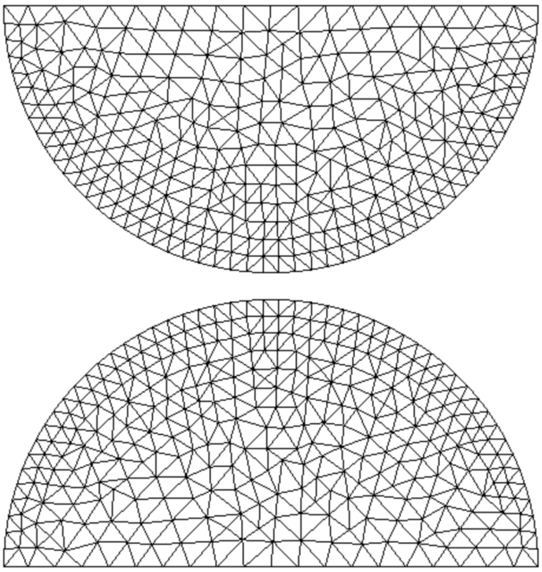

Figure 2: Half-disks of Hertz. Reference domain Ω with $R_1 = R_2 = 1$m and mesh with $\mathcal{N} = 1350$ degrees of freedom.

6.2.1 Presentation of the test cases

We consider two test cases to assess the model reduction strategy.

- Test case (a): Parametric imposed displacement (linear case)

  Let $\mathcal{P} = [0.15, 0.45]$(m) be the parameter set and consider the discrete training set $\mathcal{P}^{\text{tr}} = \{0.15 + 0.01i \mid 0 \leqslant i \leqslant 30\}$(m). Regarding boundary conditions, we consider the parametric Dirichlet condition $u_x = 0$ and $u_y = \mu/2$ on the lower horizontal edge, and the parametric Dirichlet condition $u_x = 0$ and $u_y = -\mu/2$ on the upper horizontal edge. The radii in this test case are $R_1 = R_2 = 1$m. We highlight that the symmetry of the setting and the use of matching meshes for Ω_1 and Ω_2 ensure the matching of the meshes also in the deformed configurations at equilibrium. Therefore, the gap can be computed on the reference configuration along the vertical direction. A crucial consequence is the affine character of the constraint in this test case. The left and the right panels of Figure 3 display the deformed configuration resulting from the HF displacement field for the parameter values $\mu = 0.15$m and $\mu = 0.3$m respectively,

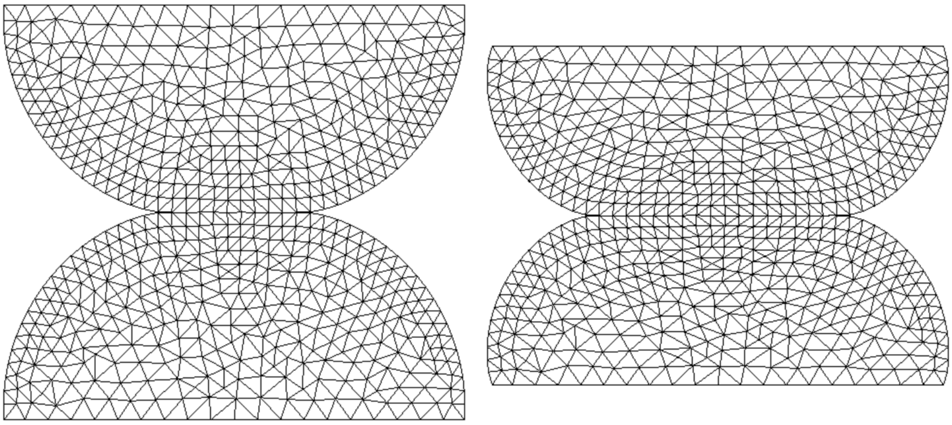

Figure 3: Test case (a) - Deformed configuration resulting from the HF displacement field $u_{\mathcal{N}}(\mu)$. Left: $\mu = 0.15$m. Right: $\mu = 0.3$m.

whereas Figure 4 displays the Lagrange multipliers (obtained with the collocation method) as a function of the abscissas in the initial configuration for some parameter values $\mu \in \mathcal{P}^{\mathrm{tr}}$. The Lagrange multipliers vanish for the nodes where the contact between the two half-disks is not established at equilibrium. As physically expected, the greater the imposed displacement, the larger the contact zone.

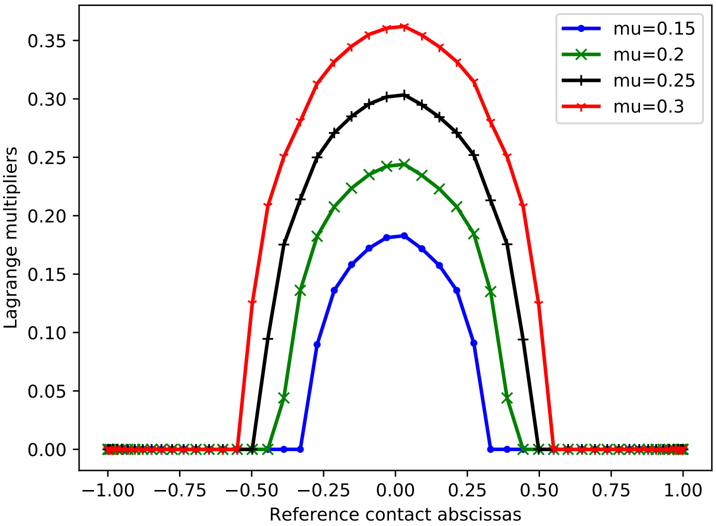

Figure 4: Test case (a) - Lagrange multipliers obtained with the collocation method as a function of the abscissas in the reference configuration for the parameter values $\mu \in \{0.15, 0.2, 0.25, 0.3\}$(m). Vanishing values correspond to nodes where the contact between the two disks is not established at equilibrium.

- Test case (b): Parametric geometry (nonlinear case)

  Consider the parameter set $\mathcal{P} = [0.9, 1.12]$(m) and the discrete training set $\mathcal{P}^{\mathrm{tr}} = \{0.905 + 0.01i |\ 0 \leqslant i \leqslant 22\}$(m). The radius of the lower disk is $R_2 = \mu$. For the boundary conditions,

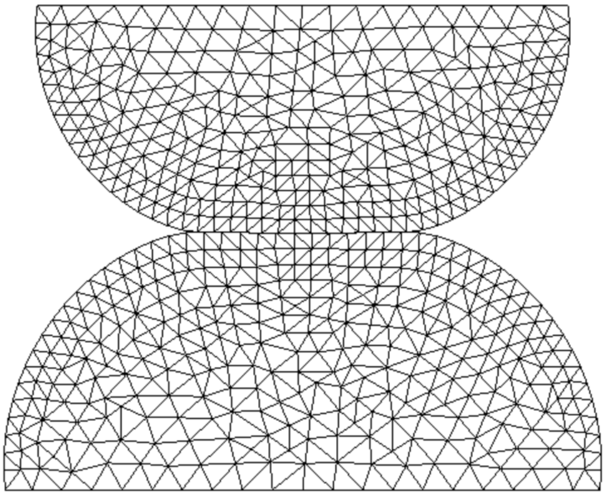

Figure 5: Test case (b) - Deformed configuration resulting from the HF displacement field $u_{\mathcal{N}}(\mu)$ for $\mu = 1.12$m.

we consider the Dirichlet condition $u_x = 0$ and $u_y = 0.2$m on the lower horizontal edge, and the Dirichlet condition $u_x = 0$ and $u_y = -0.2$m on the upper horizontal edge. Figure 5 displays the deformed configuration resulting from the HF displacement field for the parameter value $\mu = 1.12$m, whereas Figure 6 displays the Lagrange multipliers (obtained with the collocation method) as a function of the abscissas in the initial configuration for some parameter values $\mu \in \mathcal{P}^{\text{tr}}$. The Lagrange multipliers vanish on the nodes where the contact between the two half-disks is not established at equilibrium. Note that since the geometry is parameter-dependent, the meshes do not match at the contact interface.

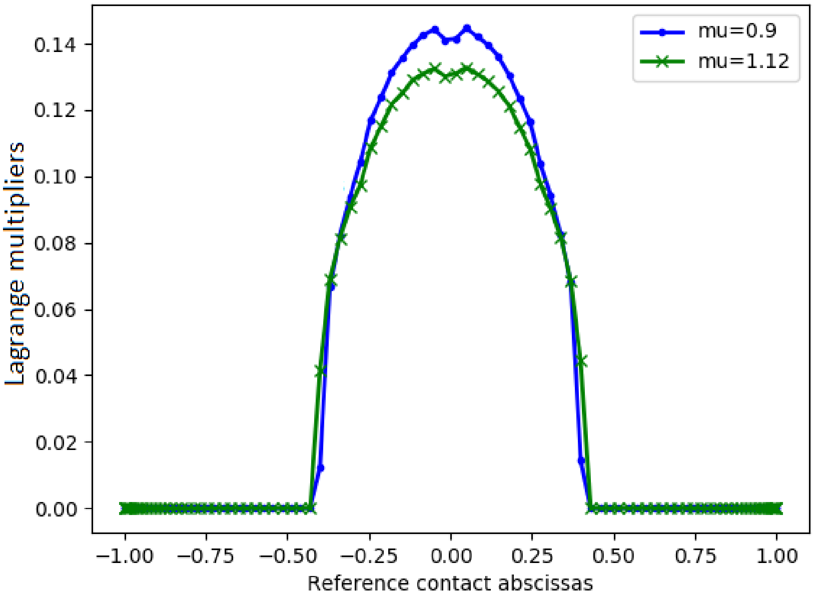

Figure 6: Test case (b) - HF Lagrange multipliers obtained with the collocation method for the parameter values $\mu \in \{0.9, 1.12\}$(m). Vanishing values correspond to nodes where the contact between the two half-disks is not established at equilibrium.

6.2.2 Choice of the HF discretization

In order to compare the collocation method with the LAC method, we consider their outputs when solving the HF problem of Hertz on the same mesh. For the Kačanov method, we use the stopping criterion

$$\max\left(\frac{\|\mathbf{u}^k(\mu)-\mathbf{u}^{k-1}(\mu)\|_{\mathbb{R}^{\mathcal{N}}}}{\|\mathbf{u}^{k-1}(\mu)\|_{\mathbb{R}^{\mathcal{N}}}},\frac{\|\boldsymbol{\lambda}^k(\mu)-\boldsymbol{\lambda}^{k-1}(\mu)\|_{\mathbb{R}^{\mathcal{R}}}}{\|\boldsymbol{\lambda}^{k-1}(\mu)\|_{\mathbb{R}^{\mathcal{R}}}}\right)\leqslant \epsilon_{\mathrm{KA}}, \tag{63}$$

with $\epsilon_{\mathrm{KA}} = 10^{-3}$. We also use a relaxation factor $\alpha = 0.3$ to improve the convergence. More specifically, at each Kačanov iteration, the primal solution $\mathbf{u}^k$ is a convex linear combination of the provisional solution $\overline{\mathbf{u}}^k$ and the previous solution $\mathbf{u}^{k-1}$, i.e. $\mathbf{u}^k = \alpha\overline{\mathbf{u}}^k+(1-\alpha)\mathbf{u}^{k-1}$. The dual solution is defined similarly. For a mesh consisting of 802 nodes, i.e. with $\mathcal{N} = 1604$ degrees of freedom, Figure 7 displays the HF normal contact stress (which is proportional to the Lagrange multipliers) for test case (b) (half-disks of Hertz with a parametric geometry) using both the LAC method and the collocation method. One can notice that the curve of the Lagrange multipliers is smoother for the collocation method, whereas that of the LAC method exhibits some irregularities. Moreover, the contact zone slightly differs between the two methods. Since the LAC method agglomerates two contact cells at a time, it involves less constraints than the collocation method. This difference results in the one-node premature ‘take-off’ for the LAC method. It can be observed at the first contact nodes starting from the left-hand side abscissas in the four panels of Figure 7. Table 1 provides the total number of Kačanov iterations for some parameter values $\mu \in \mathcal{P}^{\mathrm{tr}}$. Overall, the LAC method converges at a number of iterations which is somewhat smaller than for the collocation method. However, the collocation method enforces twice as many constraints as the LAC method.

μ		0.90	0.95	1.05	1.12
LAC	iterations	20	20	19	18
Collocation	iterations	24	24	25	24

Table 1: Test case (b) - Number of Kačanov iterations for a mesh with $\mathcal{N} = 1604$ degrees of freedom.

We run the same simulations on a finer mesh consisting of 1682 nodes, i.e., $\mathcal{N} = 3364$ degrees of freedom. We display the HF normal stress in Figure 8. As can be noticed, the curves almost overlap. Once more, we observe a slight difference at both borders of the contact zone which is two cells wider for the LAC method. The difference is less pronounced now that the mesh is finer. Another difference is that the collocation method starts to suffer from the above-mentioned oscillation phenomenon as can be seen at the reference zero abscissa on the four panels of Figure 8 (especially the first and fourth ones). We also provide the number of Kačanov iterations in Table 2. The results corroborate the previously drawn conclusions.

μ		0.90	0.95	1.05	1.12
LAC	iterations	27	19	19	20
Collocation	iterations	28	12	25	25

Table 2: Test case (b) - Number of Kačanov iterations for a mesh with $\mathcal{N} = 3364$ degrees of freedom.

In the remainder of Section 6.2, we will use the collocation method to deal with the test cases of Hertz, since we employ a rather coarse mesh on the contact zone. Instead, in Section 6.3 dealing

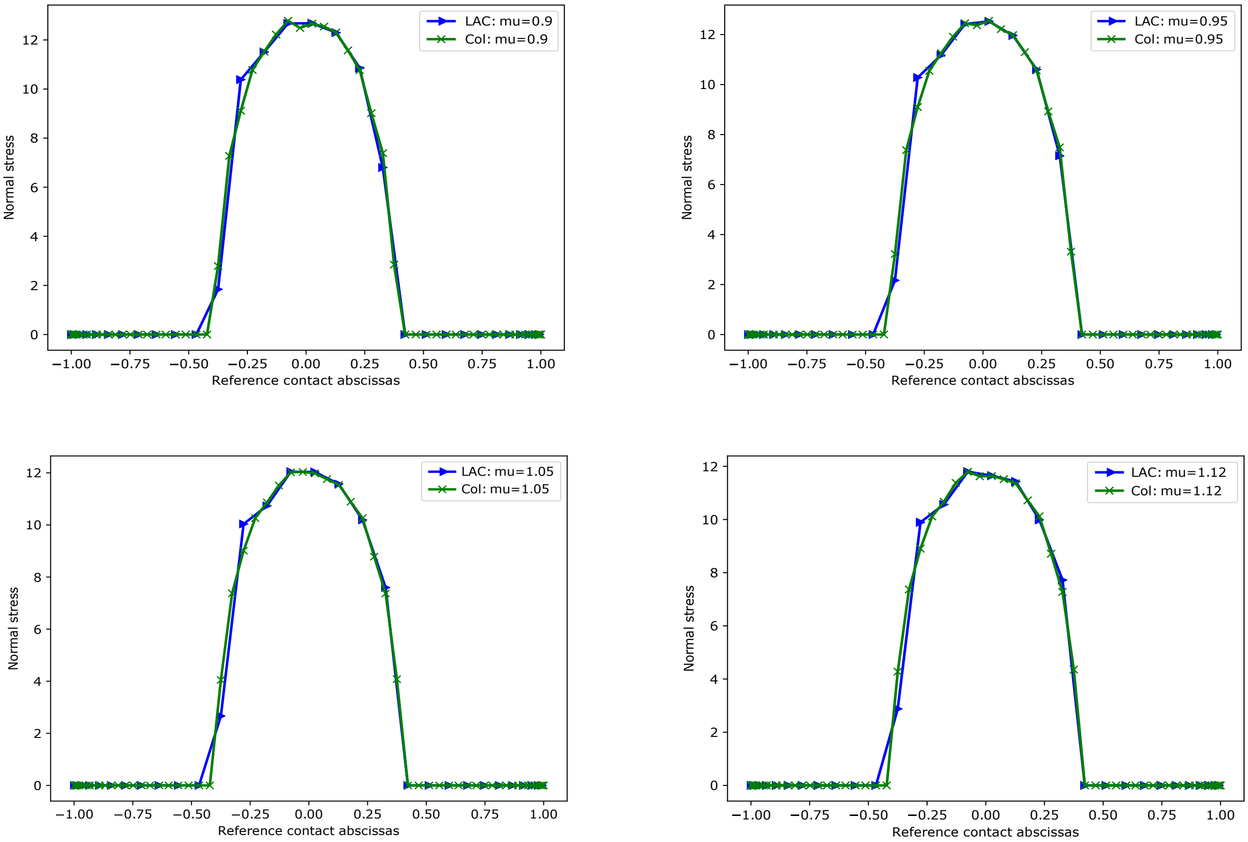

Figure 7: Test case (b) - HF normal contact stress for the LAC method (in blue) and for the collocation method 'Col' (in green) as a function of the abscissas in the reference configuration for 61 potential contact nodes. In reading order, the panels respectively correspond to the parameter values $\mu \in \{0.9, 0.95, 1.05, 1.12\}$.

with the ring-on-block test case, we will use the LAC method. We emphasize that these treatments only affect the HF solutions, so that the model reduction strategy remains unchanged in all cases.

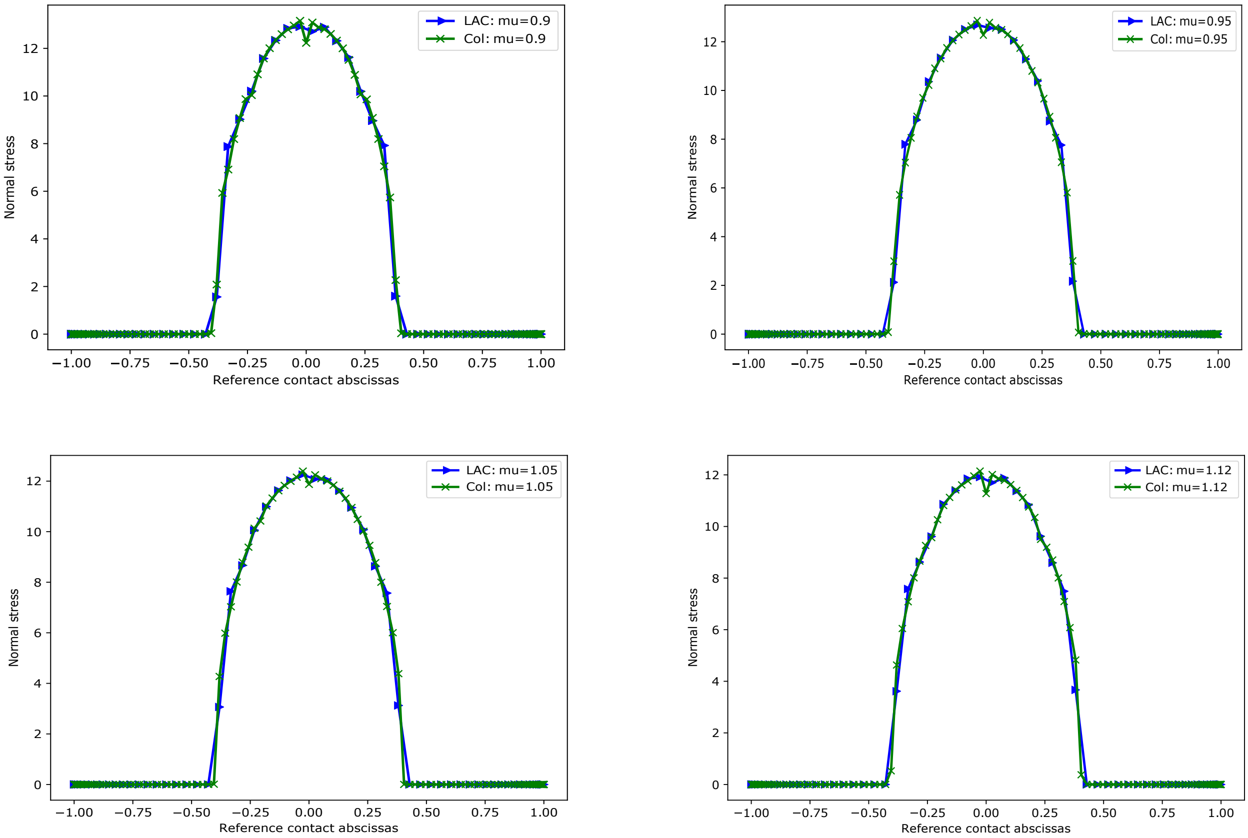

Figure 8: Test case (b) - HF normal contact stress for the LAC method (in blue) and for the collocation method 'Col' (in green) as a function of the abscissas in the reference configuration for 121 potential contact nodes. In reading order, the panels respectively correspond to the parameter values $\mu \in \{0.9, 0.95, 1.05, 1.12\}$.

6.2.3 Assessment of the RB procedure: Test case (a) - Parametric imposed displacement

During the offline stage, we perform $P = 32$ HF computations leading to the set $\mathcal{S}_{\mathrm{PRI}}$ of primal snapshots. Applying the POD to $\mathcal{S}_{\mathrm{PRI}}$ based on the energy norm and an absolute truncation threshold $\epsilon_{\mathrm{POD}} = 10^{-2}$, the primal space $\widehat{V}_N$ is composed of $N = 9$ RB functions. In order to build the dual RB cone, we test the convergence of the NMF considered in [4] and the CPG algorithm proposed herein (see Algorithm 2) using the norm $\Lambda = \|\cdot\|_{L^2(\Gamma^c)}$. The approximation errors are shown in Figure 9 for parameter values in the training set. Owing to the linearity of the constraint, the error decrease for the CPG algorithm is much faster than that of the NMF which suffers from stagnation twice. For a truncation threshold $\epsilon_{\mathrm{DU}} = 10^{-1}$, the CPG algorithm conserves seven modes, whereas the NMF achieves the same accuracy with 27 modes. Table 3 reports the dimension R of the dual RB cone $\widehat{W}_R^+$ and accuracy level ϵ_{DU} achieved by both algorithms. Note that for the CPG algorithm, ϵ_{DU} is prescribed and the number of vectors R is a result of the algorithm, whereas for the NMF, the integer R is prescribed and the accuracy can be checked *a posteriori*. The CPG algorithm outperforms the NMF with a compression level twice as good in the worst-case scenario. We define the error on the

ϵ_{DU}		10^{-1}	10^{-2}	$5 \cdot 10^{-3}$
NMF	R	27	29	31
CPG	R	7	12	16

Table 3: Test case (a) - Dual basis dimension R and accuracy level ϵ_{DU} for the NMF and the CPG algorithm with corresponding ϵ_{DU}.

minimum energy

$$e_{\text{ener}}(\mu) := \frac{1}{2} \left| a(\mu, \widehat{u}(\mu), \widehat{u}(\mu)) - f(\mu, \widehat{u}(\mu)) - a(\mu, u_{\mathcal{N}}(\mu), u_{\mathcal{N}}(\mu)) + f(\mu, u_{\mathcal{N}}(\mu)) \right|, \tag{64}$$

and the relative H^1-error error on the displacement field

$$e_{\text{displ}}(\mu) := \frac{\|\widehat{u}(\mu) - u_{\mathcal{N}}(\mu)\|_{H^1(\Omega)}}{\|u_{\mathcal{N}}(\mu)\|_{H^1(\Omega)}}. \tag{65}$$

Figure 10 compares the two errors for the CPG algorithm with $\epsilon_{\text{DU}} = 10^{-1}$ (yielding $R = 7$) and for the NMF with $R = 7$ and $R = 27$ (the latter yielding $\epsilon_{\text{DU}} = 10^{-1}$ *a posteriori*) for parameter values in the training set. As can be seen, the errors are comparable for CPG(10^{-1}) and NMF(27), although the latter uses a number of modes which is approximately four times larger than the former. However, the errors for the NMF with $R = 7$ show that, with the same number of modes as the CPG algorithm, the NMF lacks accuracy (at least half an order of magnitude).

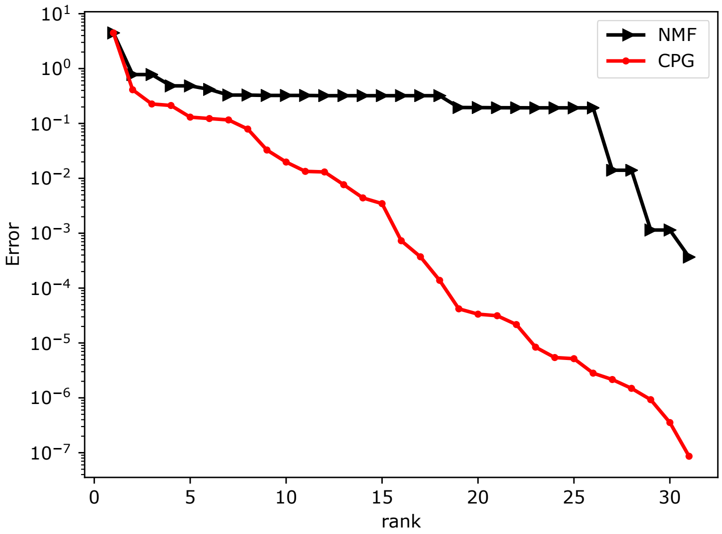

Figure 9: Test case (a) - Approximation error on the training set for the dual space $\widehat{W}_R^+$ as a function of its size R.

6.2.4 Assessment of the RB procedure: Test case (b) - Parametric geometry

During the offline stage, we perform $P = 22$ HF computations. Applying the POD to $\mathcal{S}_{\text{PRI}}$ based on the energy norm and an absolute truncation threshold $\epsilon_{\text{POD}} = 10^{-3}$, the primal space $\widehat{V}_N$ is composed

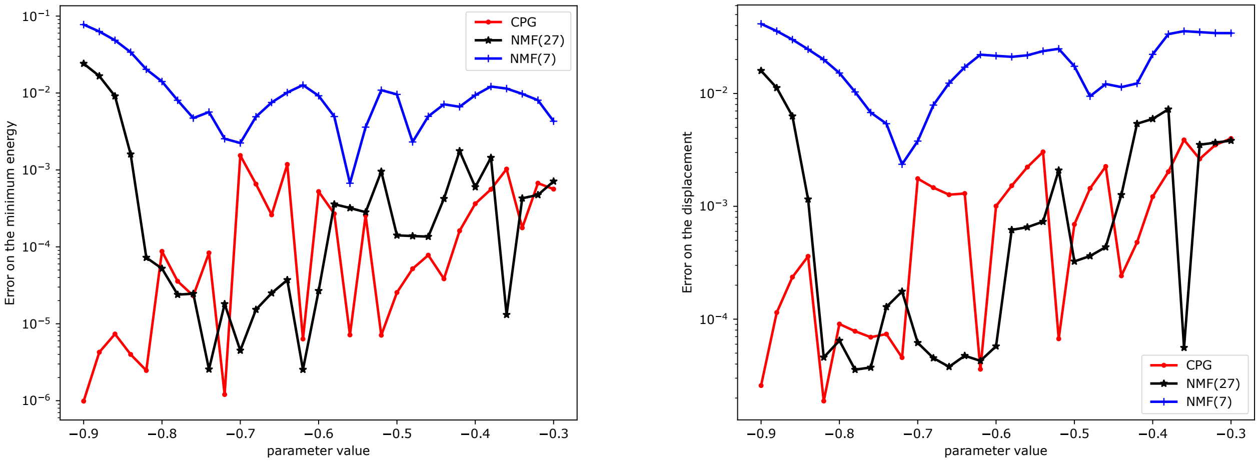

Figure 10: Test case (a) - Left: Error on the minimum energy $e_{\mathrm{ener}}(\mu)$. Right: Error on the displacement field $e_{\mathrm{displ}}(\mu)$. Parameter values in the training set. The NMF uses 27 modes whereas the CPG algorithm and the truncated NMF use 7 modes.

of $N = 11$ RB functions. Table 4 reports the size of the reduced basis as a function of the tolerance ϵ_{POD}. As can be seen, the number of offline computations is equal to the dimension of the primal space for $\epsilon_{\mathrm{POD}} = 4.10^{-6}$. The left panel of Figure 11 illustrates the decrease of the singular values associated with the POD modes. The decrease is not as sharp as is often observed for variational equalities. Moreover, the higher the rank of the singular value, the milder the decrease of the error. In order to build the dual RB cone, we test both the NMF and the CPG algorithm. Table 5 reports the dimension R of the dual RB cone $\widehat{W}_R^+$ and the accuracy level ϵ_{DU} for both algorithms. The CPG algorithm achieves the same accuracies with less basis functions than the NMF. Notice that, at the first iterations of the procedure, the NMF uses at least twice as many functions as the CPG algorithm. The right panel of Figure 11 displays the accuracy of the dual RB cone $\widehat{W}_R^+$ as its dimension R increases using the error norm $\Lambda = \|\cdot\|_{L^2(\Gamma^c)}$. This figure shows that the CPG algorithm outperforms the NMF. Note that it is actually pointless to perform an NMF with an input number

ϵ_{POD}	10^{-2}	10^{-3}	10^{-4}	10^{-5}	4.10^{-6}
N	5	11	16	20	22

Table 4: Test case (b) - Primal basis dimension N as a function of the truncation threshold ϵ_{POD}.

ϵ_{DU}		$5 \cdot 10^{-2}$	10^{-2}	$5 \cdot 10^{-3}$	10^{-3}
NMF	R	4	10	19	20
CPG	R	2	5	6	13

Table 5: Test case (b) - Dual basis dimension R and accuracy level ϵ_{DU} for the NMF and the CPG algorithm.

of modes equal to the total number of available snapshots. The same reasoning applies to the CPG algorithm as well. However, as the CPG algorithm is (in principle) steered by an accuracy threshold rather than a number of modes, the case in which all the modes are retained can still be justified.

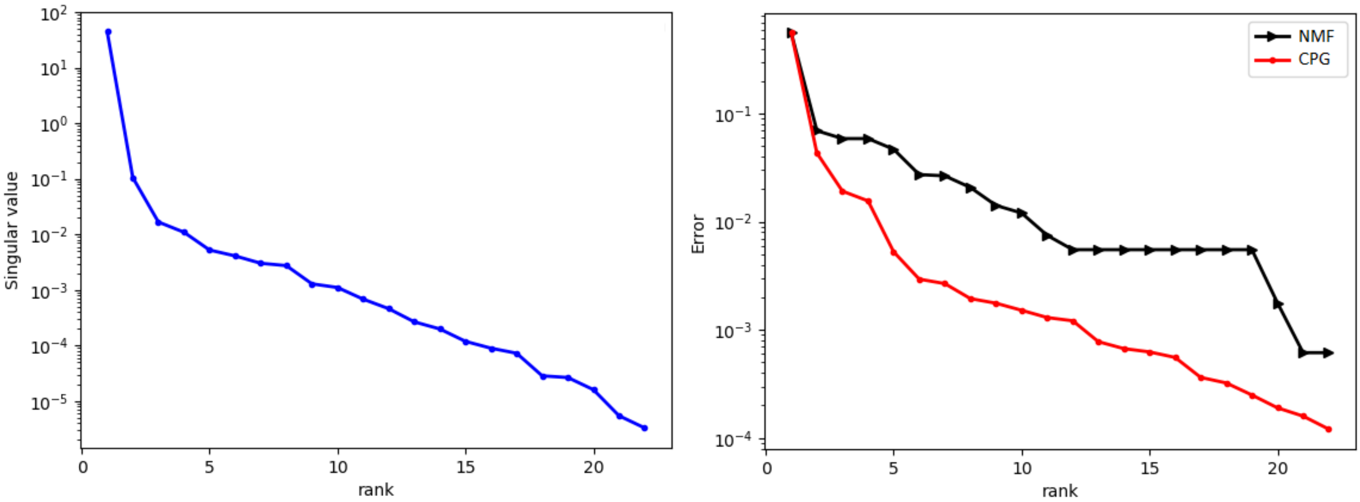

Figure 11: Test case (b) - Offline basis construction. Left: Singular values resulting from the POD using the H^1-inner product for the primal space $\widehat{V}_N$ as a function of its size N. Right: Approximation error on the training set for the dual space $\widehat{W}_R^+$ as a function of its size R.

We now perform the EIM twice so as to allow for an offline/online decomposition of both terms in the inequality constraint. The convergence of the EIM in the ℓ^∞-norm is reported in Figure 12. As can be noticed, the first selected EIM function induces a sharp decay of the initial error for the nonlinear gap mapping. In fact, the selected function corresponds to a configuration in which the contact zone is the intersection of the contact zones for all the parameters in the training set. The approximation error for the EIM decreases faster for the nonlinear gap mapping γ than for the nonlinear contact mapping κ. This observation is expected since the contact mapping is a trivariate function, whereas the gap mapping is a bivariate function. Moreover, Table 6 reports the first EIM interpolation points x_i^κ and x_i^γ. Since the effective contact zone is centered around the zero abscissa, one can notice that the selected points are chosen on the areas that do not come into contact at equilibrium. Let us physically motivate this selection for instance for the gap mapping g. In fact, g vanishes on the effective contact zone at equilibrium. Hence, an EIM function vanishing on this zone suffices to represent the effective contact nodes. However, the nodes that are less likely to come into contact have varying gap values, whence the need to interpolate over these particular points. A similar reasoning applies to the contact mapping k.

x_i^κ	-1	-0.9818	-0.7364	0.9818	-0.8136	0.9916	0.9511	-0.8477	0.7765	-0.9304
x_i^γ	1	0.9916	-1	-0.9818	-0.9976	0.9818	-0.9818	-0.9683	-0.9916	0.9062

Table 6: Test case (b) - Reference abscissas of the selected EIM interpolation points x_i^γ and x_i^κ.

Let us now investigate the online stage for the prescribed accuracy levels $\epsilon_{\text{POD}} = 10^{-5}$, $\epsilon_{\text{DU}} = 10^{-4}$, $\epsilon_{\text{EIM}}^k = 10^{-2}$, and $\epsilon_{\text{EIM}}^g = 10^{-3}$. The left panel of Figure 13 displays the error on the minimum energy

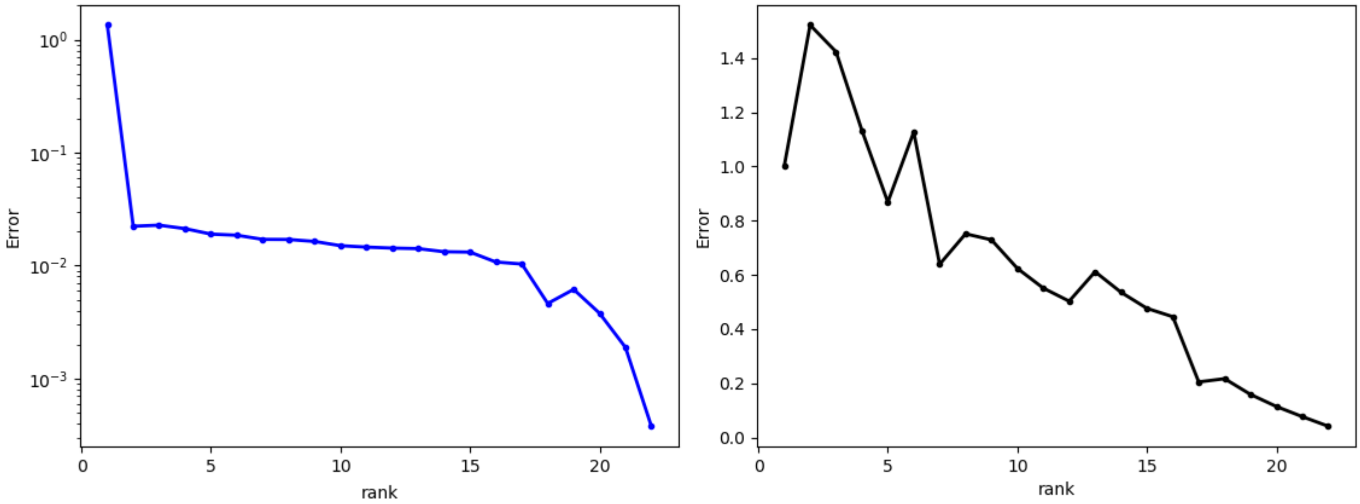

Figure 12: Test case (b) - EIM ℓ^∞-error as a function of the rank M of the EIM approximation. Left: nonlinear gap mapping γ. Right: nonlinear contact mapping κ.

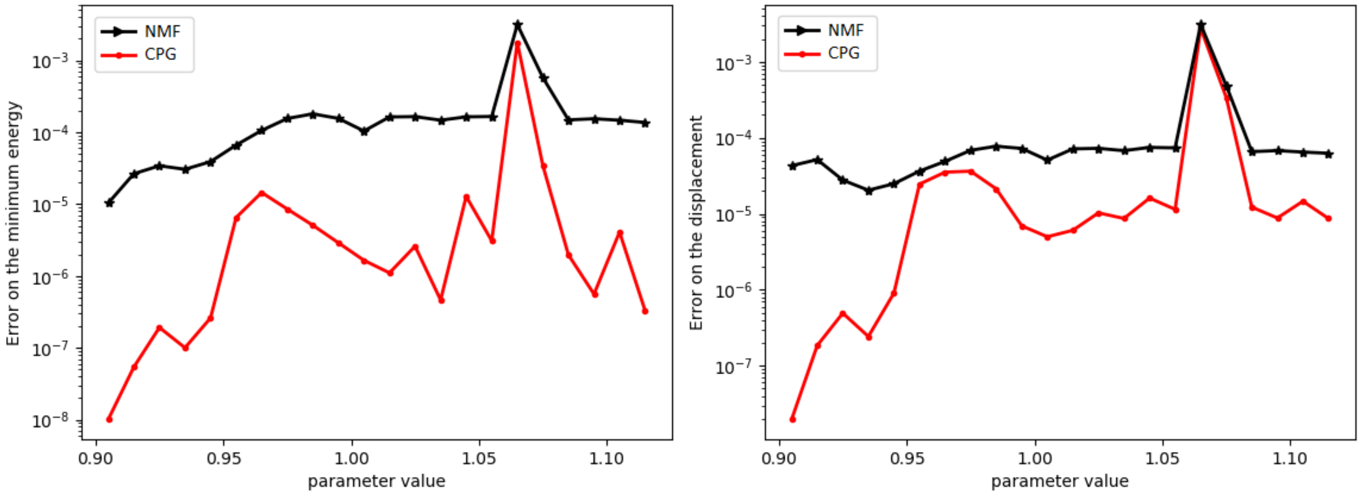

Figure 13: Test case (b) - Error quantification with accuracy levels $\epsilon_{\mathrm{DU}} = 10^{-4}$, $\epsilon^k_{\mathrm{EIM}} = 10^{-2}$, $\epsilon^g_{\mathrm{EIM}} = 10^{-3}$ and $\epsilon_{\mathrm{POD}} = 10^{-5}$. $R = 22$ for both methods. Left: Error on the minimum energy $e_{\mathrm{ener}}(\mu)$. Right: Relative H^1-error on the displacement field $e_{\mathrm{displ}}(\mu)$. Parameter values in the training set.

$e_{\mathrm{ener}}(\mu)$ for parameter values in the training set. One can notice that the error for the CPG algorithm is always below that of the NMF. Moreover, the right panel of Figure 13 shows the relative H^1-error error on the displacement field $e_{\mathrm{displ}}(\mu)$, leading to the same observations as before. Finally, Figure 14 displays a quantification of the interpenetration, i.e., the violation of the inequality constraint, by means of the error indicator

$$e_{\mathrm{inter}}(\mu) := \sqrt{\sum_{x \in \Gamma_1^{c,\mathrm{tr}}} \min\big(0, k(\mu, \widehat{u}(\mu); \widehat{u}(\mu))(x) - g(\mu, \widehat{u}(\mu))(x)\big)^2}. \tag{66}$$

For low parameter values, there is no interpenetration, but the conclusion is different for the pa-

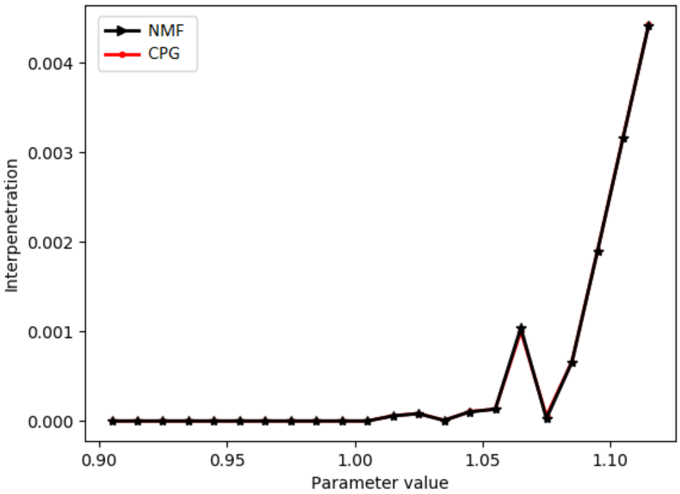

Figure 14: Test case (b) - Estimation of the interpenetration $e_{\text{inter}}(\mu)$.

rameter values that are larger than one, although the amplitude of the interpenetration remains very moderate. The reason for this is that the spatial discretization becomes coarser with the increase of the parameter value. Notice that the interpenetration curves for the NMF and the CPG almost overlap. Running both methods with the looser tolerances $\epsilon_{\text{DU}} = 1 \cdot 10^{-2}$, $\epsilon^{k}_{\text{EIM}} = 2 \cdot 10^{-1}$, $\epsilon^{g}_{\text{EIM}} = 10^{-2}$ and $\epsilon_{\text{POD}} = 10^{-2}$ produces similar results.

In order to get a clearer insight on the impact of the dual space $\widehat{W}^{+}_{R}$, we display the same plots as in the first simulation, but with the larger truncation threshold $\epsilon_{\text{DU}} = 5{\cdot}10^{-3}$. The other tolerances are as before. In this configuration, the NMF conserves $R = 18$ dual modes, whereas the CPG algorithm only conserves $R = 5$ dual modes. The minimum energy error $e_{\text{ener}}(\mu)$ and the relative H^1-error on the displacement field $e_{\text{displ}}(\mu)$ are plotted in Figure 15. In spite of the substantial difference

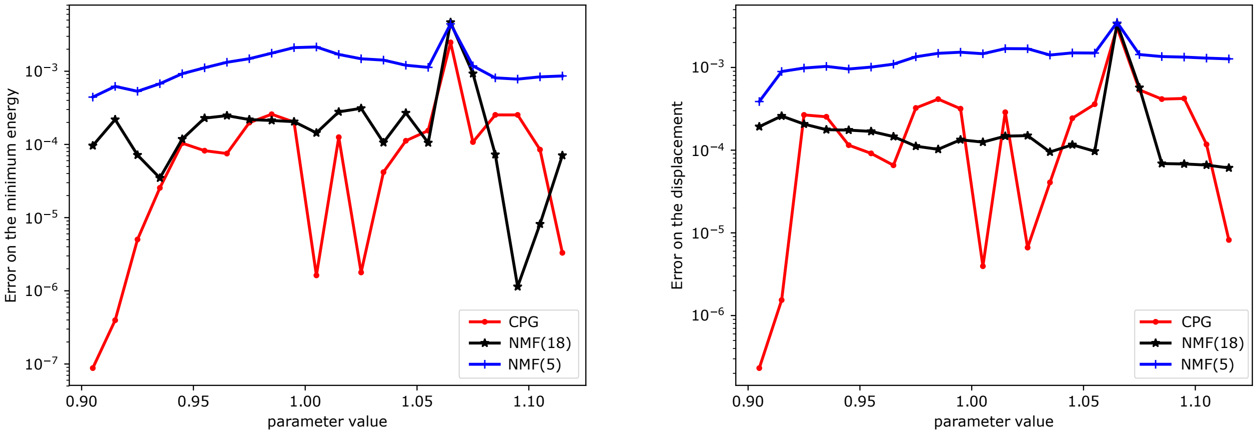

Figure 15: Test case (b) - Error quantification with accuracy levels $\epsilon_{\text{POD}} = 10^{-4}$, $\epsilon_{\text{DU}} = 5 \cdot 10^{-3}$, $\epsilon^{k}_{\text{EIM}} = 10^{-2}$, and $\epsilon^{g}_{\text{EIM}} = 10^{-4}$. The NMF uses $R = 18$ modes whereas the CPG and the truncated NMF use $R = 5$ modes. Left: Error on the minimum energy $e_{\text{ener}}(\mu)$. Right: Relative H^1-error on the displacement field $e_{\text{displ}}(\mu)$. Parameter values in the training set.

between the sizes of the NMF space and the CPG space, Figure 15 shows that the CPG algorithm still delivers accurate approximations and, in average, produces smaller errors than NMF(18). For the comparison between the two algorithms to be fairer, we also consider the case where we keep $R = 5$ basis vectors for the NMF, and we display the additional curves of the error indicators $e_{\text{ener}}(\mu)$ and $e_{\text{displ}}(\mu)$ in Figure 15 as well. In this situation, the error for the CPG algorithm is always below that of NMF(5). The quantification of the interpenetration displayed in Figure 16 corroborates the previous comments.

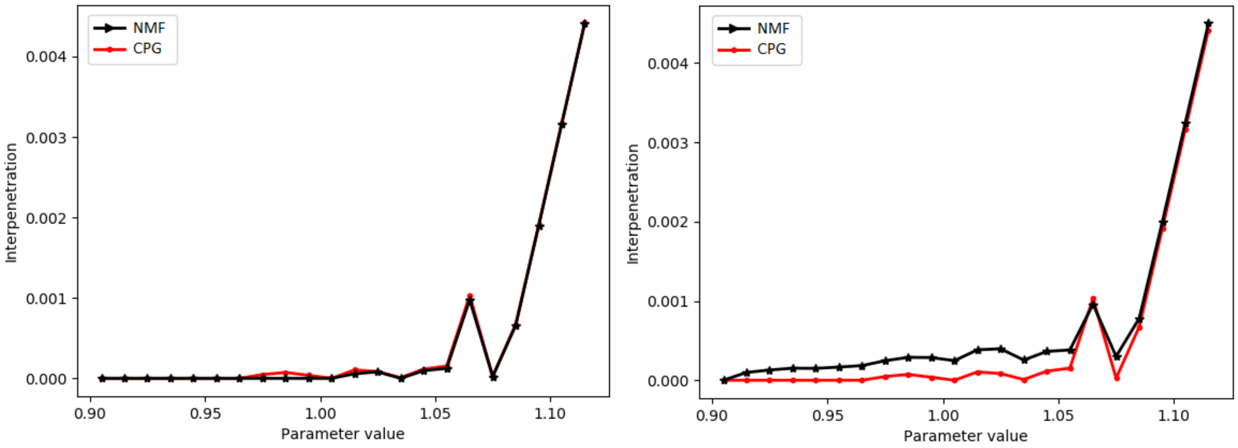

Figure 16: Test case (b) - Estimation of the interpenetration $e_{\text{inter}}(\mu)$. Left: $R = 18$ for the NMF and $R = 5$ for the CPG. Right: $R = 5$ for both algorithms.

6.3 Test case (c): Ring on block

Let $\mathcal{P}^{\text{tr}} = [0.95, 1.15](m)$ be the parameter interval and let $\mathcal{P}^{\text{tr}} = \{0.95 + 0.01i \mid 0 \leqslant i \leqslant 20\}(m)$ be the discrete training set. We investigate the case considered in [19] of an elastic ring with a parametric radius $R_1 = \mu$ that comes into contact with a rectangular block. The elastic ring has a thickness $t = 10$m and is 15 times stiffer than the block. A vertical displacement $u_y = 50$m and the homogeneous horizontal Dirichlet boundary condition $u_y = 0$ are applied to the ring at its top ends. For the lower horizontal edge of the block, we consider homogeneous Dirichlet conditions $u_x = 0$ and $u_y = 0$. The configuration Ω corresponds to the parameter value $\mu = 1$. In this test case, the non-symmetry between the two bodies is challenging since this lack of symmetry leads to non-matching meshes at the contact interface, even in the reference configuration illustrated in the left panel of Figure 17. Figure 18 displays the Lagrange multipliers (obtained with the LAC method) as a function of the abscissas in the initial configuration for two parameter values $\mu \in \mathcal{P}^{\text{tr}}$.

During the offline stage, we perform $P = 21$ HF computations. The singular values resulting from the POD applied to the collection of the primal snapshots $\mathcal{S}_{\text{PRI}}$ decrease as illustrated in the left panel of Figure 19. The right panel of Figure 19 displays the approximation error for the dual space $\widehat{W}_R^+$ as its dimension R increases using the error norm $\Lambda = \|\cdot\|_{L^2(\Gamma^c)}$. Once more, the CPG algorithm is more efficient than the NMF. As observed in the previous test cases, the latter suffers from stagnation (here, it occurs at the eighth iteration). The right panel of Figure 19 displays the approximation error for the angle-greedy algorithm. We distinguish two curves: the blue curve represents the real approximation error, i.e. that of a positive projection, whereas the green curve represents the estimated approximation error that steers the angle-greedy algorithm, i.e. that of a linear projection. Note that the estimated error is far more optimistic that the effective error. Also, the real accuracy of the angle-greedy algorithm is better than that of the NMF. Yet, the algorithm is outperformed by

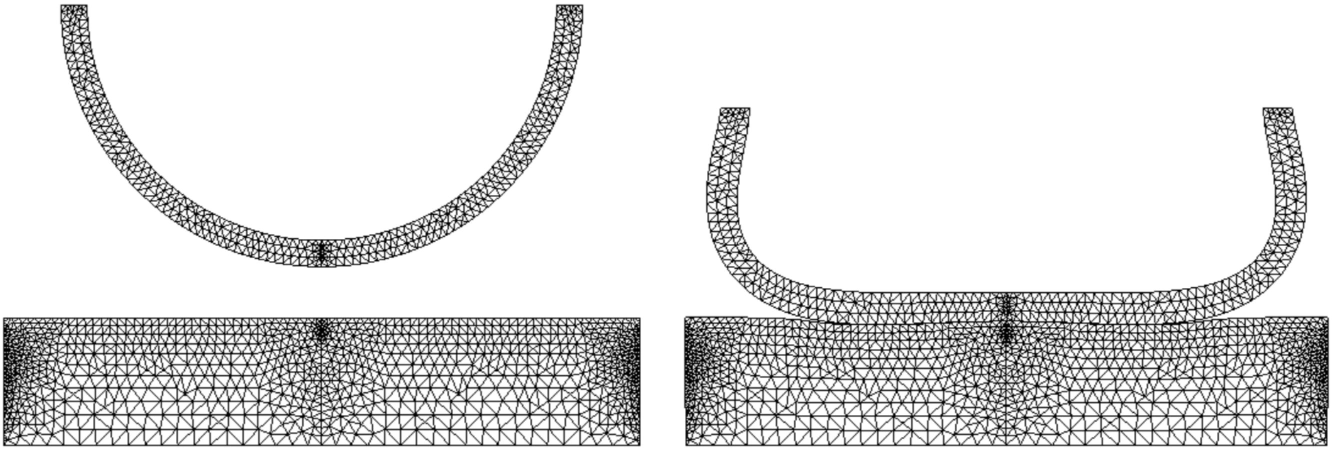

Figure 17: Test case (c) - Left: Reference domain Ω with $R_1 = 1$m and mesh with 1590 nodes. Right: Deformed configuration resulting from the HF displacement field $u_{\mathcal{N}}(\mu)$ for $R_1 = 1$m.

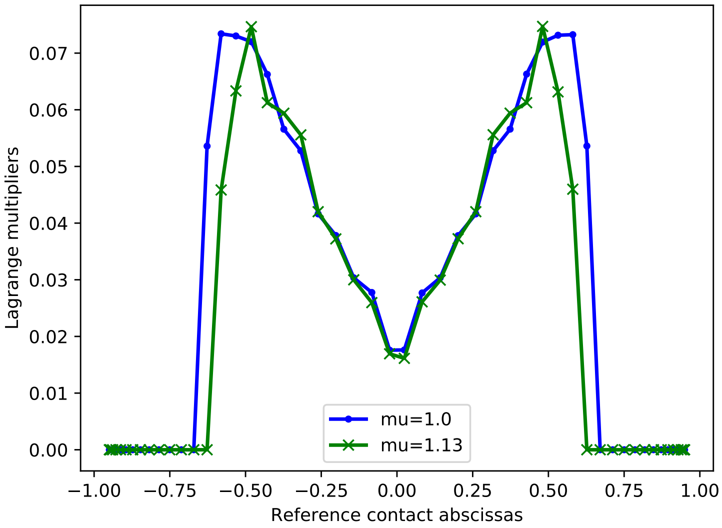

Figure 18: Test case (c) - Lagrange multipliers as a function of the abscissas in the reference configuration for the parameters $\mu \in \{1.0, 1.13\}$(m). Vanishing values correspond to nodes where the contact between the ring and the rectangular surface is not established at equilibrium.

the CPG, thereby confirming the theoretical considerations of Section 5 and Remark 6. Separately, we perform the EIM on both the contact mapping κ and the gap mapping γ. The convergence is reported in Figure 20. Afterwards, we perform the online stage for the prescribed accuracy levels $\epsilon_{\text{POD}} = 1$, $\epsilon_{\text{DU}} = 10^{-2}$, $\epsilon^{k}_{\text{EIM}} = 1$, and $\epsilon^{g}_{\text{EIM}} = 10^{-5}$. The left panel of Figure 21 displays the error on the minimum energy $e_{\text{ener}}(\mu)$, whereas the right panel shows the relative H^1-error error on the displacement field $e_{\text{displ}}(\mu)$ with parameter values in the training set. As in the previous test cases, the accuracies of the CPG algorithm using eight modes and the NMF using 21 modes are comparable. This result is confirmed when using the verification set $\mathcal{P}^{\text{verif}} = \{0.9575 + 0.02i \mid 0 \leqslant i \leqslant 10\}$ as

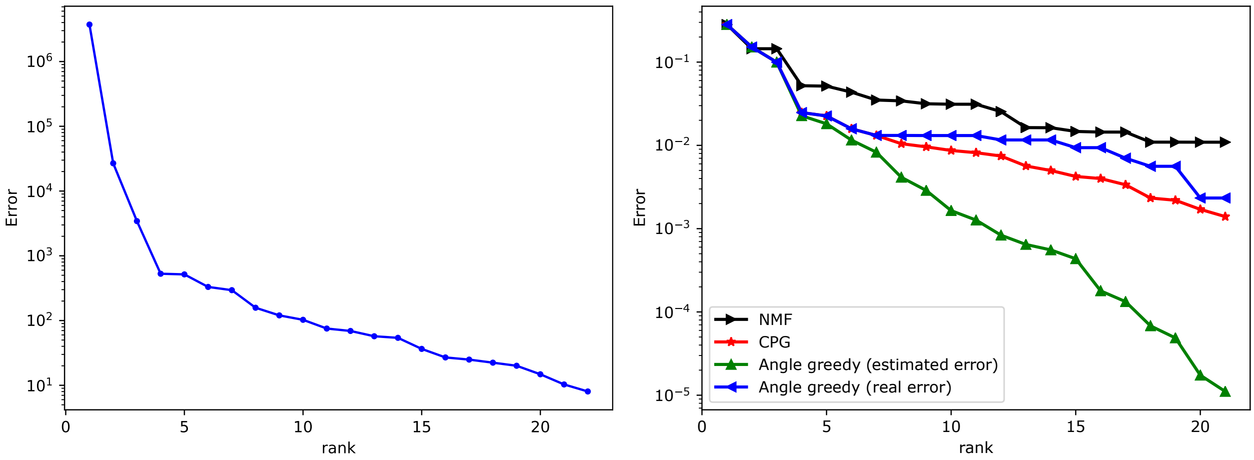

Figure 19: Test case (c) - Offline basis construction. Left: Singular values resulting from the POD for the primal space $\widehat{V}_N$ as a function of its size N. Right: Approximation error on the training set for the dual space $\widehat{W}_R^+$ as a function of its size R.

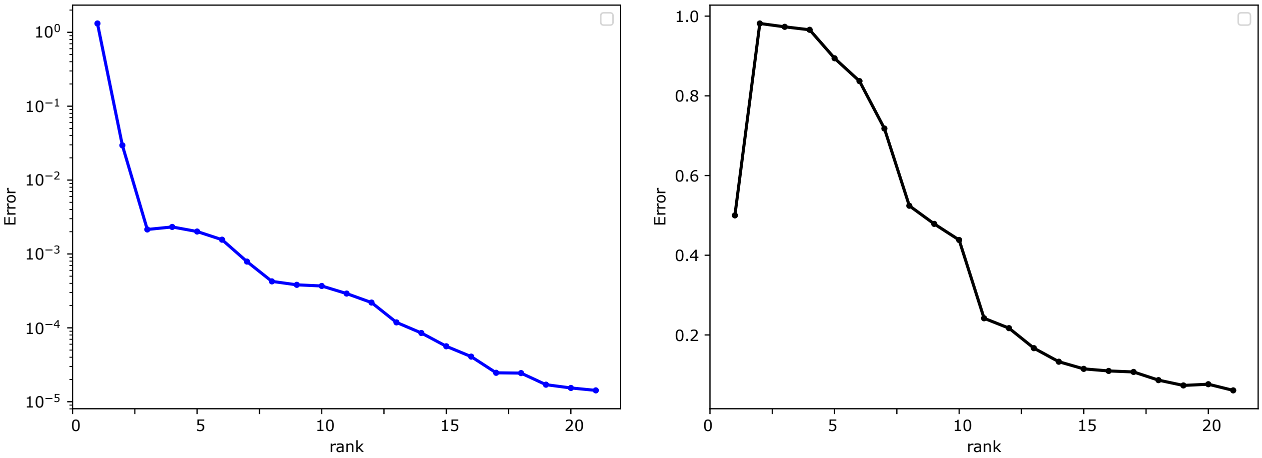

Figure 20: Test case (c) - EIM ℓ^∞-error as a function of the rank M of the EIM approximation. Left: nonlinear gap mapping γ. Right: nonlinear contact mapping κ.

illustrated in Figure 22.

7 Conclusion and perspectives

We have presented a reduced-basis scheme for parametrized nonlinear variational inequalities, which can be efficiently applied to elastic frictionless contact problems from computational mechanics. We tackled inequality constraints within the reduced basis method for a generic setting where neither small displacements nor matching meshes are assumed. Reduced basis schemes that preserve key

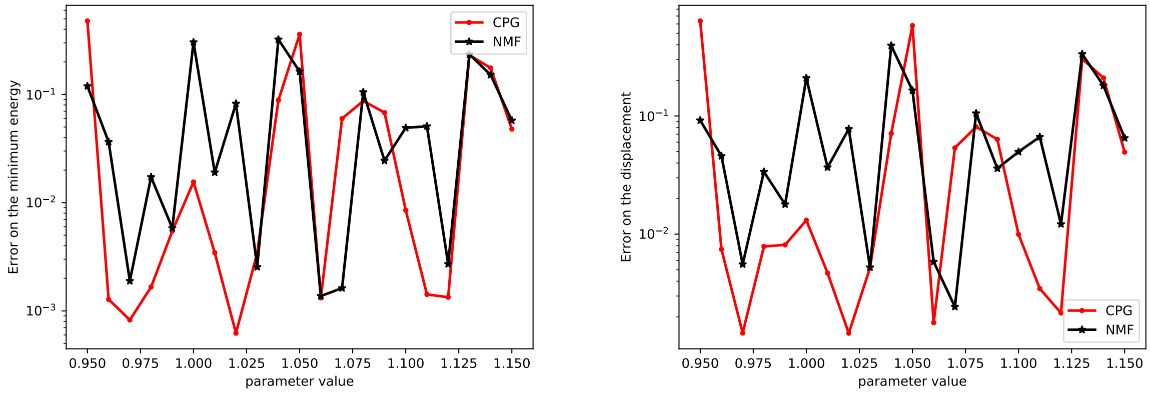

Figure 21: Test case (c) - Left: Error on the minimum energy $e_{\text{ener}}(\mu)(m)$. Right: Relative H^1-error on the displacement field $e_{\text{displ}}(\mu)$. The NMF uses 21 modes, whereas the CPG algorithm and the truncated NMF use 8 modes. Parameter values in the training set.

physical properties such as the non-negativity of the Lagrange multipliers have been achieved through a ~~novel~~ constrained greedy algorithm, which is a variant of the weak greedy algorithm based on computing orthogonal projections onto a cone. Future work includes the testing of the present methodology on three-dimensional test cases and on industrial applications. Another promising research direction is the inclusion of friction in the contact problem.

A Non-negative Matrix Factorization (NMF)

For completeness, this section provides some details on the NMF. The following results can be found in the literature on clustering [5]. The goal is to briefly describe the procedure

$$\mathbf{W} = \text{NMF}(\mathbf{T}, R), \tag{67}$$

where we are given P vectors $(\mathbf{t}_1, \cdots, \mathbf{t}_P)$ forming the rectangular matrix $\mathbf{T} \in \mathbb{R}_+^{\mathcal{R}\times P}$ whose entries are all non-negative, and we are looking for $R \leqslant \mathcal{R}$ positive vectors $(\mathbf{w}_1, \ldots, \mathbf{w}_R)$ forming the rectangular matrix $\mathbf{W} \in \mathbb{R}_+^{\mathcal{R}\times R}$. We quantify the quality of the approximation of a matrix $\mathbf{A}$ by a matrix $\mathbf{B}$ by the Frobenius norm of the difference

$$\|\mathbf{A} - \mathbf{B}\|^2 := \sum_{ij} (\mathbf{A}_{ij} - \mathbf{B}_{ij})^2. \tag{68}$$

The NMF optimization problem then reads:

$$(\mathbf{W}, \mathbf{H}) = \underset{\substack{\tilde{\mathbf{W}} \in \mathbb{R}_+^{\mathcal{R}\times R} \\ \tilde{\mathbf{H}} \in \mathbb{R}_+^{R\times P}}}{\operatorname{argmin}} \|\mathbf{T} - \tilde{\mathbf{W}}\tilde{\mathbf{H}}\|^2, \tag{69}$$

so that $\mathbf{W} \in \mathbb{R}_+^{\mathcal{R}\times R}$ and $\mathbf{H} \in \mathbb{R}_+^{R\times P}$. The functional $\|\mathbf{T} - \tilde{\mathbf{W}}\tilde{\mathbf{H}}\|$ is not convex in both variables $\tilde{\mathbf{W}}$ and $\tilde{\mathbf{H}}$ together. Thus, only the recovery of local minima is considered. Regarding the search algorithm, the decrease of the Frobenius norm is proven in [5] for the following iterative update rules:

$$\mathbf{H}_{ij} \leftarrow \mathbf{H}_{ij} \frac{(\mathbf{W}^T\mathbf{T})_{ij}}{(\mathbf{W}^T\mathbf{W}\mathbf{H})_{ij}}, \qquad \mathbf{W}_{ij}^+ \leftarrow \mathbf{W}_{ij}^+ \frac{(\mathbf{T}\mathbf{H}^T)_{ij}}{(\mathbf{W}\mathbf{H}\mathbf{H}^T)_{ij}}. \tag{70}$$

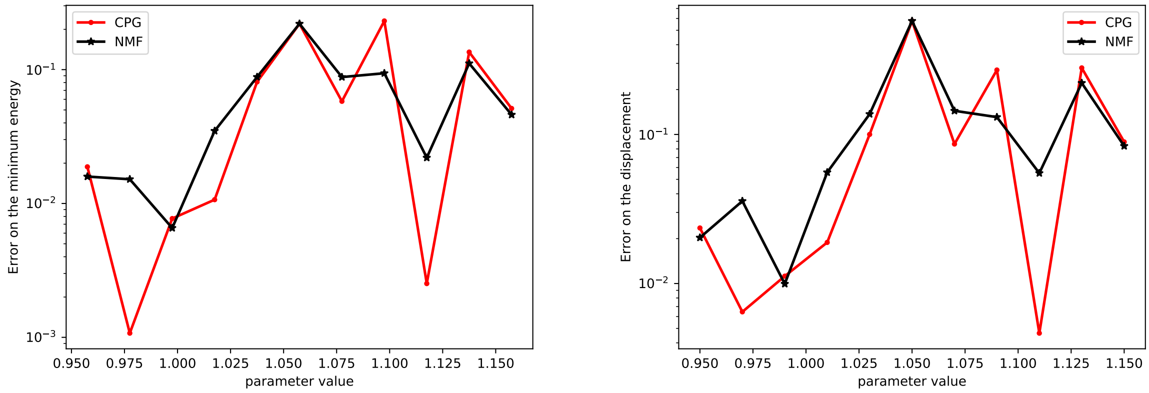

Figure 22: Test case (c) - Left: Error on the minimum energy $e_{\text{ener}}(\mu)$. Right: Relative H^1-error on the displacement field $e_{\text{displ}}(\mu)$. The NMF uses 21 modes, whereas the CPG algorithm and the truncated NMF use 8 modes. Parameter values in the verification set.

The first update rule is equivalent to a gradient descent algorithm

$$\mathbf{H}_{ij} \leftarrow \mathbf{H}_{ij} + \eta_{ij}\big((\mathbf{W}^T\mathbf{T})_{ij} - (\mathbf{W}^T\mathbf{W}\mathbf{H})_{ij}\big), \tag{71}$$

with $\eta_{ij} = \mathbf{H}_{ij}/(\mathbf{W}\mathbf{H}\mathbf{H}^T)_{ij}$. The reasoning for $\mathbf{W}_{ij}^+$ is similar. The motivation for (70) is that if the pair $(\mathbf{W}, \mathbf{H})$ yields an exact reconstruction, i.e. $\mathbf{T} = \mathbf{W}\mathbf{H}$, then $(\mathbf{W}, \mathbf{H})$ is a fixed-point of the algorithm. Finally, note that, in contrast to the POD, the integer R is a required input for the NMF. Moreover, the uniqueness of the output is not guaranteed. In fact, any positive matrix $\mathbf{D} \in \mathbb{R}^{R\times R}$ satisfies $\mathbf{T} = \mathbf{W}\mathbf{D}\mathbf{D}^{-1}\mathbf{H}$, thereby leading to another NMF decomposition.

References

[1] J. S. Hesthaven, G. Rozza, and B. Stamm, Certified reduced basis methods for parametrized partial differential equations. SpringerBriefs in Mathematics, Springer, Cham; BCAM Basque Center for Applied Mathematics, Bilbao, 2016.

[2] A. Quarteroni, A. Manzoni, and F. Negri, Reduced basis methods for partial differential equations. La Matematica per il 3+2, Springer International Publishing, 2016.

[3] B. Haasdonk, J. Salomon, and B. Wohlmuth, “A reduced basis method for parametrized variational inequalities,” SIAM J. Numer. Anal., vol. 50, no. 5, pp. 2656–2676, 2012.

[4] M. Balajewicz, D. Amsallem, and C. Farhat, “Projection-based model reduction for contact problems,” Internat. J. Numer. Methods Engrg., vol. 106, no. 8, pp. 644–663, 2016.

[5] D. D. Lee and H. S. Seung, “Algorithms for non-negative matrix factorization,” in Proceedings of the 13th International Conference on Neural Information Processing Systems, NIPS’00, (Cambridge, MA, USA), pp. 535–541, MIT Press, 2000.

[6] J. Fauque, I. Ramière, and D. Ryckelynck, “Hybrid hyper-reduced modeling for contact mechanics problems,” Internat. J. Numer. Methods Engrg., vol. 115, no. 1, pp. 117–139, 2018.

[7] S. Glas and K. Urban, "On noncoercive variational inequalities," SIAM Journal on Numerical Analysis, vol. 52, pp. 2250–2271, 01 2014.

[8] S. Glas and K. Urban, "Numerical investigations of an error bound for reduced basis approximations of noncoercice variational inequalities," IFAC-PapersOnLine, vol. 48, pp. 721–726, 12 2015.

[9] Z. Zhang, E. Bader, and K. Veroy, "A Duality Approach to Error Estimation for Variational Inequalities," arXiv, 2014.

[10] E. Bader, Z. Zhang, and K. Veroy, "An empirical interpolation approach to reduced basis approximations for variational inequalities," Math. Comput. Model. Dyn. Syst., vol. 22, no. 4, pp. 345–361, 2016.

[11] Z. Zhang, E. Bader, and K. Veroy, "A slack approach to reduced-basis approximation and error estimation for variational inequalities," C. R. Math. Acad. Sci. Paris, vol. 354, no. 3, pp. 283–289, 2016.

[12] O. Burkovska, Reduced Basis Methods for Option Pricing and Calibration. PhD thesis, Technische Universität München, 2016.

[13] O. Burkovska, B. Haasdonk, J. Salomon, and B. Wohlmuth, "Reduced basis methods for pricing options with the Black–Scholes and Heston models," SIAM Journal on Financial Mathematics, vol. 6, 08 2014.

[14] B. Haasdonk, J. Salomon, and B. Wohlmuth, "A reduced basis method for the simulation of american options," Numerical Mathematics and Advanced Applications, 01 2012.

[15] A. Giacoma, D. Dureisseix, A. Gravouil, and M. Rochette, "Vers une approche PGD quasi-optimale pour les problèmes nonlinéaires de contact frottant," in 12e Colloque national en calcul des structures, (Giens, France), CSMA, May 2015.

[16] M. Barrault, Y. Maday, N. C. Nguyen, and A. T. Patera, "An 'empirical interpolation' method: application to efficient reduced-basis discretization of partial differential equations," C. R. Math. Acad. Sci. Paris, vol. 339, no. 9, pp. 667–672, 2004.

[17] Y. Maday, N. C. Nguyen, A. T. Patera, and G. S. H. Pau, "A general multipurpose interpolation procedure: the magic points," Commun. Pure Appl. Anal., vol. 8, no. 1, pp. 383–404, 2009.

[18] H. Hertz, "Über die Berührung fester elastischer Körper," Journal für die reine und angewandte Mathematik, vol. 1882, no. 92, pp. 156–171, 1882.

[19] P. Wriggers, Computational Contact Mechanics. Wiley, 2002.

[20] A. Ern and J.-L. Guermond, Theory and practice of finite elements, vol. 159 of Applied Mathematical Sciences. Springer-Verlag, New York, 2004.

[21] S. Fučík, A. Kratochvíl, and J. Nečas, "Kačanov-Galerkin method and its application," Acta Universitatis Carolinae. Mathematica et Physica, vol. 15, no. 1, pp. 31–33, 1974.

[22] A. Benaceur, Model reduction for nonlinear thermics and mechanics. Phd thesis, University Paris-Est Marne la Vallée, Dec. 2018.

[23] B. Haasdonk, “Convergence rates of the POD-greedy method,” ESAIM Math. Model. Numer. Anal., vol. 47, no. 3, pp. 859–873, 2013.

[24] M. Hinze and S. Volkwein, “Proper orthogonal decomposition surrogate models for nonlinear dynamical systems: error estimates and suboptimal control,” in Dimension reduction of large-scale systems, vol. 45 of Lect. Notes Comput. Sci. Eng., pp. 261–306, Springer, Berlin, 2005.

[25] K. Kunisch and S. Volkwein, “Galerkin proper orthogonal decomposition methods for parabolic problems,” Numer. Math., vol. 90, no. 1, pp. 117–148, 2001.

[26] M. S. Andersen, J. Dahl, and L. Vandenberghe, “Cvxopt: A python package for convex optimization.” Open source on `http://www.abel.ee.ucla.edu/cvxopt`, 2008.

[27] F. Hecht, “New developments in freefem++.” Open source on `http://www.freefem.org`, 2012.

[28] G. Drouet and P. Hild, “An accurate local average contact method for nonmatching meshes,” Numer. Math., vol. 136, no. 2, pp. 467–502, 2017.